Astronomy & Astrophysics

Herschel-ATLAS and ALMA

HATLAS J142935.3-002836, a lensed major merger at redshift 1.027

Hugo Messias[1,2], Simon Dye[3], Neil Nagar[1], Gustavo Orellana[1], R. Shane Bussmann[4], Jae Calanog[5],
Helmut Dannerbauer[6], Hai Fu[7], Edo Ibar[8], Andrew Inohara[5], R. J. Ivison[9,10], Mattia Negrello[11],
Dominik A. Riechers[12,13], Yun-Kyeong Sheen[1], James E. Aguirre[14], Simon Amber[15], Mark Birkinshaw[16,17],
Nathan Bourne[3], Charles M. Bradford[18], Dave L. Clements[19], Asantha Cooray[5,12], Gianfranco De Zotti[11],
Ricardo Demarco[1], Loretta Dunne[20,9], Stephen Eales[21], Simone Fleuren[22], Julia Kamenetzky[23], Roxana E. Lupu[14],
Steve J. Maddox[20,9], Daniel P. Marrone[24], Michał J. Michałowski[9], Eric J. Murphy[25], Hien T. Nguyen[18],
Alain Omont[26], Kate Rowlands[27], Dan Smith[28], Matt Smith[21], Elisabetta Valiante[21], and Joaquin D. Vieira[29]

(Affiliations can be found after the references)

ABSTRACT

Context. The submillimetre-bright galaxy population is believed to comprise, aside from local galaxies and radio-loud sources, intrinsically active star-forming galaxies, the brightest of which are lensed gravitationally. The latter enable studies at a level of detail beyond what is usually possible by the observation facility.

Aims. This work focuses on one of these lensed systems, HATLAS J142935.3−002836 (H1429−0028), selected in the *Herschel*-ATLAS field. Gathering a rich, multi-wavelength dataset, we aim to confirm the lensing hypothesis and model the background source's morphology and dynamics, as well as to provide a full physical characterisation.

Methods. Multi-wavelength high-resolution data is utilised to assess the nature of the system. A lensing-analysis algorithm that simultaneously fits different wavebands is adopted to characterise the lens. The background galaxy dynamical information is studied by reconstructing the 3D source plane of the ALMA CO (J:4 → 3) transition. Near-IR imaging from HST and Keck-AO allows to constrain rest-frame optical photometry independently for the foreground and background systems. Physical parameters (such as stellar and dust masses) are estimated via modelling of the spectral energy distribution taking source blending, foreground obscuration, and differential magnification into account.

Results. The system comprises a foreground edge-on disk galaxy (at $z_{\rm sp} = 0.218$) with an almost complete Einstein ring around it. The background source (at $z_{\rm sp} = 1.027$) is magnified by a factor of $\mu \sim 8-10$ depending on wavelength. It is comprised of two components and a tens-of-kpc-long tidal tail resembling the Antennæ merger. As a whole, the background source is a massive stellar system ($1.32^{+0.63}_{-0.41} \times 10^{11}\,M_\odot$) forming stars at a rate of $394 \pm 90\,M_\odot\,{\rm yr}^{-1}$, and it has a significant gas reservoir $M_{\rm ISM} = 4.6 \pm 1.7 \times 10^{10}\,M_\odot$. Its depletion time due to star formation alone is thus expected to be $\tau_{\rm SF} = M_{\rm ISM}/{\rm SFR} = 117 \pm 51\,{\rm Myr}$. The dynamical mass of one of the components is estimated to be $5.8 \pm 1.7 \times 10^{10}\,M_\odot$, and, together with the photometric total mass estimate, it implies that H1429−0028 is a major merger system ($1{:}2.8^{+1.8}_{-1.5}$).

Key words. gravitational lensing: strong – galaxies: ISM – galaxies: kinematics and dynamics

1. Introduction

Most of the sources responsible for the far-infrared (FIR) background (Reach et al. 1995; Puget et al. 1996; Fixsen et al. 1998; Lagache et al. 1999) are at $z > 1$ (Franceschini et al. 1994; Fall et al. 1996; Burigana & Popa 1998; Hauser & Dwek 2001). Their detailed study has been limited by instrumental development: early submillimetre (submm; rest-frame FIR) studies were based on shallow- and low-resolution surveys (e.g., Scott et al. 2002; Smail et al. 2002; Greve et al. 2004, 2008; Magnelli et al. 2009; Clements et al. 2010; Dannerbauer et al. 2010; Jacobs et al. 2011), but the advent of *Herschel* and the construction of the Atacama Large (sub-)Millimetre-Array (ALMA) are overcoming these limitations.

These recent instrumental developments have enabled systematic, detailed follow-up of the brightest of the galaxies detected in the FIR and (sub-)millimetre regime (e.g., Cox et al. 2011; Harris et al. 2012; Karim et al. 2012; Lupu et al. 2012; Ivison et al. 2013; Hodge et al. 2013; Vieira et al. 2013; Weiß et al. 2013; Riechers et al. 2013), revolutionising our view of

this galaxy population (for a review, see Casey et al. 2014). Commonly referred to as submm galaxies (SMGs), they are believed to be a sporadic (∼100 Myr, Greve et al. 2005; Tacconi et al. 2006, 2008) and extremely active phase of evolution (star-formation rates of $\sim 10^2-10^3\,M_\odot\,{\rm yr}^{-1}$, Ivison et al. 2000; Chapman et al. 2005; Coppin et al. 2008; Michałowski et al. 2010a,b; Wardlow et al. 2011; Yun et al. 2012; Smolčić et al. 2012; Riechers et al. 2013). Whether this phase is responsible for the formation of the bulk of the stellar population of their descendants is still a matter of debate (Renzini 2006; Tacconi et al. 2008; González et al. 2011), as is the trigger for this extreme phase. Gas-rich major mergers (Frayer et al. 1998, 1999; Ivison et al. 2000; Tacconi et al. 2008; Daddi et al. 2010b; Engel et al. 2010; Menéndez-Delmestre et al. 2013), smooth accretion of cold gas as suggested by hydrodynamical simulations (Kereš et al. 2005; Carilli et al. 2010; Davé et al. 2010; Hayward et al. 2011; Hodge et al. 2012) and self-regulated baryon collapse (Granato et al. 2004; Lapi et al. 2011) have all been proposed to induce the SMG phase.

Article published by EDP Sciences

Distinguishing between, for instance, a merger event and a gas-rich clumpy disk is not trivial, since the latter may resemble a merger system in low-resolution imaging and/or in case no velocity information is available. Hence, especially at high redshift (when disk galaxies are believed to be clumpy), spectral and spatial detail are key (e.g., Förster Schreiber et al. 2009, 2011; Swinbank et al. 2011; Riechers et al. 2011; Ivison et al. 2013). While spectral capabilities are limited by technology, in some cases spatial resolution is boosted by nature. These cases occur when a deep gravitational potential (e.g., a galaxy over-density or an isolated massive galaxy) modifies the light path from a background source, inducing brightness and spatial magnification. This gravitational lensing (GL) boosts the sensitivity and resolution of our telescopes, allowing a more direct comparison with the local galaxy population (see discussion in Meylan et al. 2006). It is thus no surprise that GL has allowed breakthrough science in the study of distant galaxies via significantly improved detection limits and spatial resolutions (e.g., Blain 1996; Smail et al. 2002; Kneib et al. 2005; Solomon & Vanden Bout 2005; Knudsen et al. 2006; Tacconi et al. 2006; Swinbank et al. 2010).

Until recently, finding these rare lensed systems required deliberate searches through known galaxy over-densities where the probability of GL is higher (Smail et al. 1997; Postman et al. 2012; Furlanetto et al. 2013). However, follow-up observations of the brightest sources in under-dense regions revealed evidence of GL (e.g., Chapman et al. 2002). With the advent of wide-area (hundreds of square degrees) FIR and submm surveys, combined with powerful follow-up facilities, many such GL cases have been confirmed. This has led to simple criteria allowing efficient GL selection. Based on a small subset of bright galaxies found in the *Herschel*-Astrophysical TeraHertz Large Area Survey (*H*-ATLAS, ~570 deg^2, Eales et al. 2010), Negrello et al. (2010) show that a simple flux cut at $500\,\mu m$ ($S_{500\,\mu m} > 100$ mJy), followed by optical/near-IR/radio imaging analysis to discard local and radio-bright sources, is a highly efficient technique to select GL systems. Since then, more than 20 of these systems have been confirmed in *Herschel* surveys (e.g., Conley et al. 2011; Fu et al. 2012; Bussmann et al. 2012; Wardlow et al. 2013; George et al. 2013; Calanog et al. 2014). In parallel, observations undertaken at 1.4 mm on the South Pole Telescope have provided a large population of GL systems (Vieira et al. 2013; Weiß et al. 2013).

The size of the GL sample now allows a systematic investigation of the properties of the lenses and background objects (e.g., Ivison et al. 2010; Frayer et al. 2011; Vieira et al. 2013; Weiß et al. 2013; George et al. 2014), allowing direct comparison with similarly luminous local galaxies. In this work, we have obtained Atacama Large Millimetre Array (ALMA) observations of one of the lensed sources found in the *H*-ATLAS, H1429−0028, as part of this continued effort to increase the number of GL systems with high-spatial-resolution molecular data, which is still relatively scarce. With its improved detection, spectral and resolving capabilities, ALMA enables a fast and detailed view of the gas and dust in distant lensed sources, not only spatially, but also spectroscopically (Vieira et al. 2013; Weiß et al. 2013). This pilot study, combining *Herschel* and ALMA with GL, illustrates the promise of this fusion to unravel the physical processes that dominate the distant submm Universe.

The work is organised as follows. Section 2 describes the source selection and the plethora of data supporting this work, Sect. 3 presents the results directly obtained from the data described in the previous section, in Sect. 4 the lensing analysis is presented along with the physical properties of both fore- and background systems, Sect. 5 finishes with the main conclusions

from this work. Throughout this work we adopt the following ΛCDM cosmology: $H_0 = 70$ km s^{-1} Mpc^{-1}, $\Omega_M = 0.3$, $\Omega_\Lambda = 0.7$, and a Chabrier initial mass function (considering a stellar mass range of 0.1 to 100 $M_\odot$).

2. Source selection and observations

2.1. Source selection

HATLAS J142935.3−002836, alias H1429−0028, the focus of this study, was identified in the H-ATLAS coverage of the GAMA 15-hr field. With a submm flux of $S_{500\,\mu m} = 227 \pm 8$ mJy, it is considerably brighter than the flux cut proposed by Negrello et al. (2010, $S_{500\,\mu m} > 100$ mJy) to select candidate sources for gravitationally lensed systems. This source, in particular, was found to be a $160\,\mu m$-peaker, suggesting $z \sim 1$. The SPIRE data reduction is described in Pascale et al. (2011), while source extraction and flux density estimation are described in Rigby et al. (2011).

2.2. Optical spectroscopy

Long-slit spectroscopic observations at the Gemini-South telescope were taken using the Gemini Multi-Object Spectrograph-South (GMOS-S) instrument on the night of 2012 February 25 as part of program GS-2012A-Q-52 (P.I. Bussmann). Four exposures of 15 min each were made through a 1″ slit with the B600 grating. Dithering was used in both the wavelength direction and along the slit to minimise the effects of bad columns and gaps between the GMOS-S chips. The central wavelengths for the two observations were 520 and 525 nm, and flat-field observations were interspersed between the observations at each wavelength setting. Wavelength calibration was achieved using CuAr arc lamp exposures, taken using the same instrumental set-up as for the science exposures. This provided a spectral resolution of ≈0.62 Å. A position angle of 70° east of north was used, and the detector was binned by 4 pixels in both the spectral and spatial directions.

We processed the data using standard IRAF GMOS-S reduction routines. Since the primary aim of these observations was to obtain a spectroscopic redshift, flux calibration was not performed. We used the *xcsao* routine in IRAF to measure the spectroscopic redshift.

2.3. Hubble Space Telescope F110W

A SNAPshot observation was obtained with the *Hubble* Space Telescope[1] (HST) on 2011 December 28th, as part of Cycle-19 proposal 12488 (P.I. Negrello), using Wide-Field Camera 3 (WFC3) with its wide *J* filter, *F110W*. The total exposure time was 252 s. Data were processed using the PyRAF Astrodrizzle package. Individual frames were corrected for distortion, cleaned of cosmic rays and other artifacts and median combined. The resulting ~2′ × 2′ image was re-sampled to a finer pixel scale of 0.0642″. The FWHM is 0.17″ as measured from a stellar source in the observed field.

2.4. Keck Telescope adaptive optics H and K_s

We obtained sub-arcsec resolution images of H1429−0028 in the H and K_s bands with the Keck-II laser-guide-star adaptive-optics system (LGSAO; Wizinowich et al. 2006). The observations took place on 2012 Feb. 4 UT with the NIRC2 wide camera (0.04″ pixel^{-1}) under excellent conditions (program ID: U034N2L; P.I. Cooray). The only suitable tip-tilt star had $R = 15.2$ and lay 78″ north-east of H1429−0028. In order to fit the star within the vignetted field for the tip-tilt sensor, we had to rotate the camera to a PA of 259.6 deg and offset H1429−0028 from the centre to the top-right part of the detector. We obtained 15 useful 80-s exposures in K_s and 10 useful 120-s exposures in H.

We used custom IDL scripts to reduce the images, following standard procedures. Briefly, after bad pixel masking, background subtraction, and flat-fielding, sky background and object masks were updated iteratively. For each frame, after subtracting a scaled median sky, the residual background was removed with 2-dimensional B-spline models. In the last iteration, we discarded frames of the poorest image quality and corrected the camera distortion using the on-sky distortion solution from observations of the globular cluster M 92[2]. The resolution of the final image is 0.11″ and 0.13″ in FWHM for the H and K_s images, respectively, as measured from two stellar sources <21″ from H1429−0028. The two sources were nevertheless faint, and the PSF was approximated by a Gaussian with the referred widths.

2.5. Spitzer IRAC 3.6 and 4.5 μm

3.6- and 4.5-μm images were acquired using the Infrared Array Camera (IRAC, Fazio et al. 2004) aboard *Spitzer* (Werner et al. 2004) on 2012 September 27th as part of the Cycle 8 GO program 80156 (P.I. Cooray). The imaging involved a 38-position dither pattern, with a total exposure time of just over 1 ks, reaching r.m.s. depths of 3.3 and 3.6 μJy at 3.6 and 4.5 μm, respectively. Corrected basic calibrated data, pre-processed by the *Spitzer* Science Center, were spatially aligned and combined into mosaics with a re-sampled pixel size of 0.6″ and angular resolution of 2−2.5″, using version 18.5.0 of MOPEX (Makovoz & Marleau 2005). These data were then used for photometric measurements.

2.6. Jansky Very Large Array 7 GHz

High-resolution 7-GHz continuum data were acquired using National Radio Astronomy Observatory's Janksy Very Large Array[3] (JVLA) during 2011 June (proposal 11A-182; P.I. Ivison), in A configuration, with 64×2-MHz channels in each of two intermediate frequencies (IFs), each IF with dual polarisation, recording data every 1 s. 1505+0306 was observed every few minutes to determine complex gain solutions and bandpass corrections; 3C 286 was used to set the absolute flux density scale. Using natural weighting, the resulting map has a 0.4″ × 0.3″ FWHM synthesised beam and an r.m.s. noise level of 10 μJy beam^{-1}.

2.7. Z-SPEC on APEX

H1429−0028 was observed with Z-SPEC mounted on the 12-m APEX telescope on 2−5 January 2011 as part of the *H*-ATLAS and Universidad de Concepción collaboration (projects C-087.F-0015B-2011, P.I. Orellana, and projects 087.A-0820 and 088.A-1004, P.I. Ivison), during the APEX P87 and P88 periods under excellent weather conditions (PWV ∼ 0.6, ranging from 0.2 to 0.9).

Antenna pointing calibrations were performed a few times each night using a bright planet or quasar near the target producing typically ≲4″ corrections. Telescope focus was adjusted once each day, just after sunset, and little variation was seen throughout the observing run. To remove atmospheric fluctuations, we used a wobbler at 1.8 Hz to switch the signal to a blank field 45″ away. Data were taken in chunks of 20 s.

Taking into account gain factors, the signal from each spectral channel was flux calibrated using observations of Uranus. This is done by building a model of the flux conversion factor (from instrument Volts to Jy) as a function of each detector's mean operating (DC) voltage (Bradford et al. 2009). Second-order pixel-to-pixel spectral variations (≲5%) were corrected using a compilation of observations of flat-spectrum sources (J1337−130 and J1229+021 in this case). The spectra are considerably noisier at the lowest frequencies due to the pressure-broadening of a water line at 183 GHz.

All errors are propagated to the source calibration using a customised pipeline developed to reduce Z-SPEC data while mounted at the Caltech Submillimetre Observatory (e.g., Bradford et al. 2009; Scott et al. 2011; Lupu et al. 2012; Zemcov et al. 2012).

The total integration time on source was 8.1 h, reaching a sensitivity of 0.8 Jy s$^{1/2}$ at the bandwidth centre. The rms uncertainty on the final co-added spectrum ranges from 5 to 10 mJy.

2.8. CARMA

We used CARMA (Bock et al. 2006) to observe the CO($J = 2 \rightarrow 1$) transition ($\nu_{\rm rest} = 230.5380$ GHz) towards H1429−0028 (proposal CX322, P.I. Riechers). Based on the APEX/Z-Spec redshift of $z_{\rm spec} = 1.026$, observations were made using the 3 mm receivers with the CARMA spectral line correlator set to an effective bandwidth of 3.7 GHz per sideband (IF range: 1.2−4.9 GHz) at 5.208 MHz (6.8 km s^{-1}) spectral resolution, placing the redshifted CO($J = 2 \rightarrow 1$) line at an IF frequency of 3.6 GHz in the upper sideband. Observations were carried out under good 3-mm weather conditions on 2011 January 16 in a hybrid configuration between the B and E arrays (only data from 9 antennas on short baselines are used), yielding an on-source (total) observing time of 2.9 h (4.4 h; equivalent to 1.0 h on source with the full 15 antenna array). The nearby quasar J1512−090 was observed every 20 min for complex gain calibration. Pointing was performed at least every 2−4 h on nearby stars and radio quasars, using both optical and radio modes. The bandpass shape and absolute flux density scale were derived from observations of the bright quasar, 3C 273. The resulting calibration is expected to be accurate to ∼15%.

The MIRIAD package was used for data processing and analysis. The calibrated data were imaged using natural weighting, resulting in a synthesised beam of 7.1″ × 6.1″, and an rms noise of 2.6 mJy beam^{-1} over 281.25 MHz (365.7 km s^{-1}).

2.9. MAMBO-2 on IRAM-30 m

We measured the 1.2 mm continuum flux density of H1429−0028 using the 117-channel bolometer array, MAMBO-2, at the IRAM 30 m telescope (Dannerbauer et al., in prep.). In January 2011, the target was observed twice, each time for 8 min, in the photometric mode of MAMBO-2. This observing mode, so-called "on-off", is based on the chop-nod technique where the target is placed on a reference bolometer element (on-target channel). With a beam size of $\approx 11''$ at 1.2 mm, the continuum emission is accurately measured given the much smaller size of the source (Sect. 3.1). Standard calibration techniques and sources − including pointing, focus and flux calibration − were used. Data were processed with MOPSIC, an upgrade of the MOPSI software package (Zylka 1998).

2.10. ALMA

H1429−0028 was observed by ALMA as part of the project 2011.0.00476.S (ALMA Cycle 0; P.I. Orellana). Data from two of the five approved "science goals" − Band 3 (centred at 107 GHz) and Band 6 (234 GHz) − were observed during shared-risk time (Cycle 0) and form the core of this publication. The remaining three science goals in our proposal were not observed successfully by the end of Cycle 0.

All spectral windows (four in each set-up) were set in frequency division mode (FDM) with a 1.875-GHz bandwidth (0.488 MHz channel width), equivalent to $\sim$2400 km s^{-1} ($\sim$0.6 km s^{-1}) and $\sim$5350 km s^{-1} ($\sim$1.4 km s^{-1}) in Bands 3 and 6, respectively. The tuning was based on the CARMA redshift estimate of $z = 1.0271$ (Sect. 3.4). The total on-source integration time was about 30 min in each band. Titan was used as a flux calibrator and J1256−057 (3C 279) as a bandpass calibrator. The phase calibrator, J1408−078, was observed every $\sim$14 min in Band 3 and every $\sim$12 min in Band 6.

Data processing was done using CASA[4]. Initial calibration, including water vapour radiometer (WVR) corrections, phase and amplitude calibrations, were performed by the ALMA science operations team during quality assurance (QA). Our team checked the phase and amplitude steps of the calibration, and re-processed the data taking into account the new Butler-JPL-Horizons 2012 models.

2.10.1. Band 3

Of the two approved Band-3 science goals, only one was observed. In this science goal, the first spectral window was centred at 113.7341 GHz to cover the ^{12}CO (J:2 → 1) transition (rest-frame 230.538 GHz). The remaining three spectral windows were tuned to trace continuum emission at 100.879 GHz, 102.121 GHz, and 112.235 GHz (rest-frame 204.482, 207.000, and 227.500 GHz, respectively).

This science goal was executed twice. The first execution was on 2012 May 9 with 16 antennas in the Cycle-0 "extended configuration". Two of the 16 antennas presented visible spikes in their bandpass and the data from these antennas were deleted. To conform with the Cycle-0 specifications on the minimum number of antennas, a second execution of the science goal was made on 2012 July 28. Here, the 25 antennas were in an improved Cycle-0 "extended configuration", with baselines between $\sim$20 m and $\sim$450 m. Data from one antenna, DV02, was flagged by the ALMA science operations team; antenna DV08 presented a large amplitude scatter and its data were therefore also flagged.

The six observations of the phase calibrator reveal clean phase solutions with minimal phase variations ($<$8° over 14 min) for all antennas. In two spectral windows tracing the continuum, the bandpass calibrator presented line features, necessitating the deletion of these channels. The final combined uv dataset, based on the two observation runs, allows the source to be imaged at a resolution of $\sim$1.88″ × 1.25″ (natural weighting) or $\sim$1.57″ × 1.12″ (uniform weighting). The source, with a maximum extension of $\sim$2″, fits well within the primary beam of the ALMA 12 m antennas at this frequency ($\sim$58″), so no relative flux corrections are required across the field.

2.10.2. Band 6

The Band-6 science goal was executed on 2012 April 23, with 17 ALMA antennas in the Cycle 0 "extended configuration" (maximum baseline of $\sim$400 m). The adopted setup included four spectral windows: SPW0, with central frequency 242.802 GHz, was centred on C I ^{3}P$_1$ → ^{3}P$_0$ (rest frequency 492.161 GHz); SPW1, with central frequency, 241.614 GHz, was centred on CS (J:10 → 9, rest frequency 489.751 GHz); SPW2, with central frequency 227.450 GHz, was centred on CO (J:4 → 3, rest frequency, 461.041 GHz), previously detected by APEX/Z-SPEC; SPW3 was centred at 225.950 GHz in order to trace the source continuum. The choice of SPW tuning involved the line of interest, even though this meant some overlap of the SPWs and thus some loss of sensitivity for continuum images.

At these frequencies, Titan is clearly resolved by the longest baselines, hence the flux of the phase calibrators was determined in a subset of short-baseline antennas. Titan showed line emission in one spectral window, and the affected channels were flagged. Channels affected by atmospheric emission were also flagged. The six observations of the phase calibrator revealed clean phase solutions with minimal phase variations ($<$8° over 10 min) for all antennas. All SPW3 data from one antenna, DV05, were flagged.

The final uv dataset, based on 16 antennas with a maximum baseline of 400 m, allowed the source to be imaged at a resolution of $\sim$0.81″ × 0.58″ (natural weighting) or $\sim$0.63″ × 0.54″ (uniform weighting). Again, no relative pointing flux corrections are required across the field. One self-calibration run was done using the CO (J:4 → 3) map in order to further correct phase-delays on this dataset, improving the image quality[5].

2.11. Data from wide-field surveys

Given the wealth of deep wide-area surveys available today, more multi-wavelength photometry information were found in the following surveys: Sloan Digital Sky Survey (SDSS, York et al. 2000), VISTA Kilo-Degree Infrared Galaxy survey (VIKING, Sutherland 2012), Wide-Field Infrared Survey Explorer (WISE, Wright et al. 2010), and H-ATLAS (Eales et al. 2010). From these surveys we obtained $ugriz$ (SDSS), $ZYHJK_s$ (VIKING), 3.4−22 μm (WISE), and 100−500 μm (H-ATLAS) photometry. We discuss the flux density measurements obtained from these datasets in Sect. 3.7.

---

[4] http://casa.nrao.edu

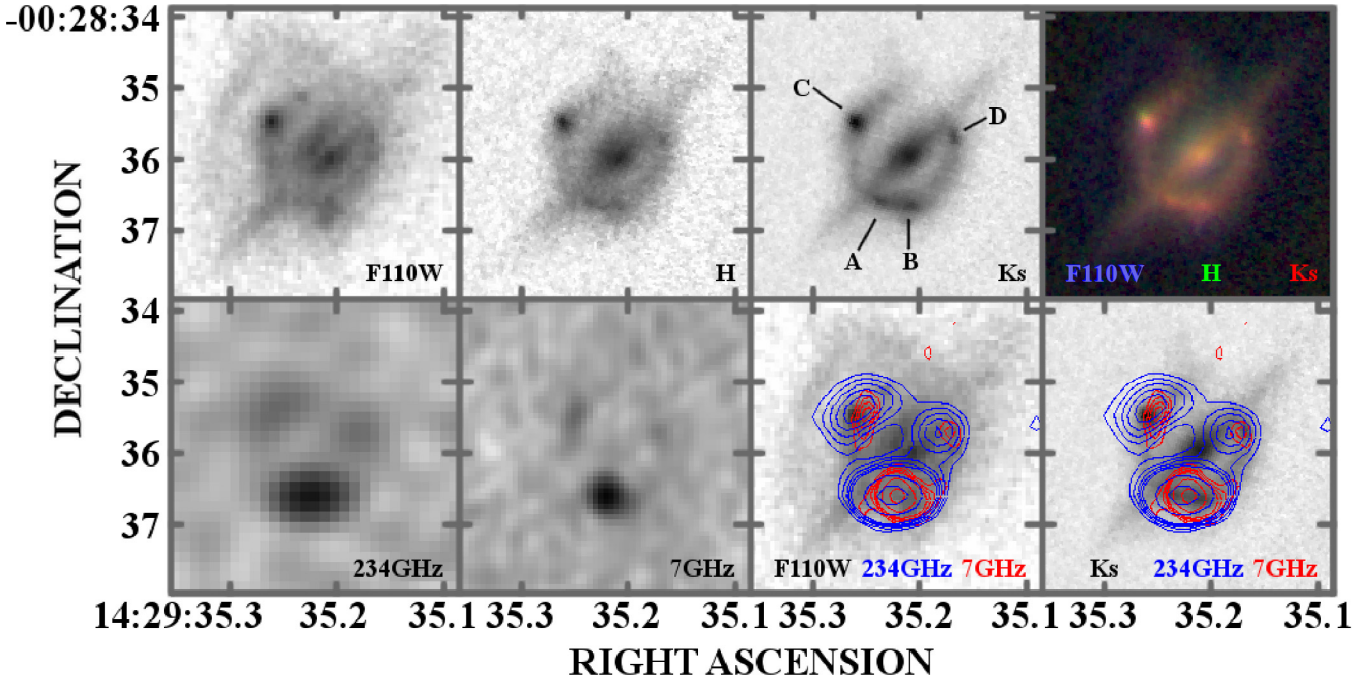[5] Further runs finding phase or amplitude solutions did not yield significant improvement.

Fig. 1. Multi-wavelength morphology of the H1429−0028 system. Images are 4″ in size. North is up; east is left. Both the foreground galaxy and the lensed galaxy − in the form of an Einstein-ring − are detected and resolved in the near-IR high-resolution imaging (*top-row*; $F110W$, H, and K_s are displayed with an $a \sin h$ scale, but with different flux ranges). The knot nomenclature adopted throughout the paper is indicated in the K_s imaging. *Top-right panel* shows a near-IR colour image (displayed with a *sqrt* scale; images combined with the same flux range). Two *bottom-left panels* show ALMA 234- and JVLA 7-GHz continuum maps (restored with uniform and Briggs robust = 0.5 weightings, respectively). These are compared against $F110W$ and K_s morphologies in the *two bottom-right panels*. Blue contours (at 3σ, $\sqrt{2}$-increments up to 675 μJy beam^{-1}, 15σ, and 25σ, with $\sigma = 78\,\mu$Jy beam^{-1}) refer to the 234 GHz continuum, while red contours (at 3σ, $\sqrt{2}$-increments up to 72 μJy beam^{-1}, 15σ, and 30σ, with $\sigma = 10\,\mu$Jy beam^{-1}) refer to the 7 GHz continuum.

3. Results

3.1. Multi-wavelength morphology

In general, seeing-limited ground-based observations of H1429−0028 reveal an almost point-like source. Resolving the system requires space-based, adaptive-optics- (AO-) assisted, or interferometric observations (Sect. 2). Figure 1 shows a colour image of the system, made using HST-$F110W$ (blue), Keck-AO H (green) and K_s (red) imaging. These data clearly reveal a foreground source with a bulge+disk morphology, and an almost complete Einstein ring with a diameter of ∼1.4″. We identify four possible knots: two in the southern region (knots A and B); one in the north-east (knot C) and one in the north-west region (knot D).

The HST imaging shows an additional faint arc-like feature extending from north to east, ∼1.5″ from the centre of the ring. The HST $F110W$ filter covers the 460−678 nm rest-frame spectral range of the background source ($z_{\rm spec} = 1.027$, Sect. 3.3), which includes potentially bright emission lines like H$_\alpha$, so the arc could trace an extended region of star formation.

The JVLA observation of 7-GHz continuum and the ALMA observation of CO(4 → 3) and 234-GHz continuum also provide resolved imaging of the system (see the two bottom left-hand panels in Fig. 1). The JVLA and ALMA continuum maps are overlaid as contours on the HST $F110W$ and the Keck AO K_s images (two bottom right-hand panels in Fig. 1). The morphologies closely match each other, with A and B knots appearing as one. The slight offset on knot D may result from centroid position uncertainty due to the low-signal-to-noise detection, but it can also be real since different components are being traced in each dataset.

Although the morphology at rest-frame optical may hint at a quad-lens system, this is only observed in the K_s-band. Restoring the JVLA map with Briggs weighting (robust = 0), yielding a beam size of 0.29″ × 0.26″ does not confirm the quad-lens morphology[6]. Also, the relative brightness of the knots are not consistent with a simple quad-lens system, nor is there a relative-knot-flux match between the optical and mm-to-cm spectral regimes. This hints at an extended background source or a multiple-source background system, or effects induced by the foreground system. This will be discussed in Sect. 4.1.

3.2. Optical spectroscopy

The Gemini-South optical spectroscopy (Sect. 2.2 and Fig. 2) shows the clear detection of the Ca H and K absorption lines and an [O II] emission line. For a template, we used a 5-Gyr-old simple stellar population from Bruzual & Charlot (2003) with solar metallicity. While this template does not perfectly match the lensing galaxy spectra, it is sufficient to determine a precise redshift. The corresponding spectroscopic redshift of the lensing galaxy is $z = 0.21844 \pm 0.00046$ based on the Ca absorption lines, where the error refers to the instrumental uncertainty alone.

3.3. Z-SPEC on APEX

The APEX/Z-Spec spectrum of H1429−0028 is shown in Fig. 3. The two reliably-detected lines are identified as CO (J:4 → 3)

---

[6] Further increasing the resolution yields too noisy a map to draw any conclusion.
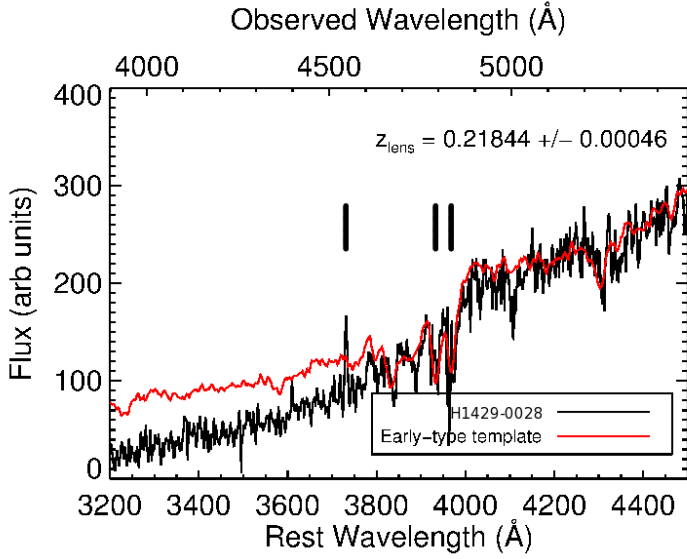
Fig. 2. Foreground spectrum observed with GMOS-S at Gemini-South. The black line shows the observed spectrum, while the overlaid red line shows the best-fit early-type template. The three vertical lines indicate the wavelengths of the [O II] and Ca H and K lines.
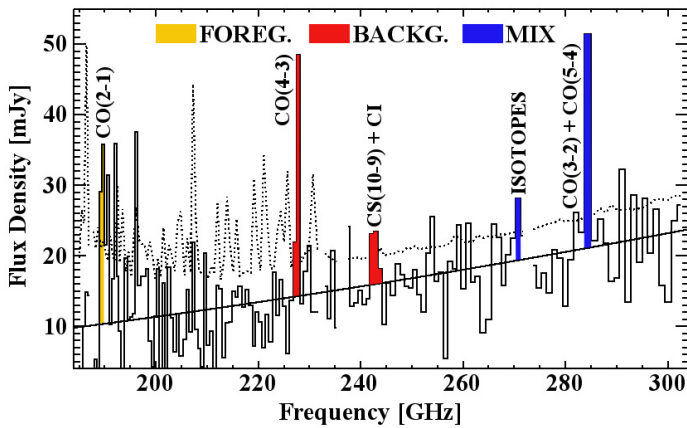

Fig. 3. Z-Spec spectrum of H1429-0028 with observed frequency on the x-axis and flux density (mJy) on the y-axis. Reliably detected lines include CO (J:4 → 3) and CO (J:5 → 4) at $z = 1.026 \pm 0.002$. The channel where CO (J:5 → 4) from the background source is observed is likely contaminated by CO (J:3 → 2) from the foreground source. Colours represent channels with line emission from the foreground source (yellow), background source (red), or a mix from both (blue, see text for more details). The solid line shows the fit to the continuum, while the dashed line represents the 1σ error above the continuum.

and CO (J:5 → 4), yielding a redshift of 1.026 ± 0.002 for the background source. The integrated fluxes are $37.6 \pm 8.8 \, \mathrm{Jy \, km \, s^{-1}}$ for CO (J:4 → 3), and $40.0 \pm 5.9 \, \mathrm{Jy \, km \, s^{-1}}$ for CO (J:5 → 4). The continuum was considered to be power-law ($f \propto \nu^\alpha$) with a spectral-index of $\alpha = 1.76 \pm 0.23$.

The redshift of the foreground source implies that the CO (J:3 → 2) transition falls on the same Z-SPEC channel as the background CO (J:5 → 4) emission (at an expected frequency separation of $\Delta \nu \sim 0.4 \, \mathrm{GHz}$). Also, the foreground CO (J:2 → 1) emission line falls in a very noisy part of the spectrum (at 189 GHz), showing a detection significance level of $\sim 2.8\sigma$ ($32.9 \pm 11.7 \, \mathrm{Jy \, km \, s^{-1}}$). Attempting to constrain the flux of the foreground CO (J:3 → 2) transition provides a broad flux range ($4.2 \pm 1.5 - 32.9 \pm 11.7 \, \mathrm{Jy \, km \, s^{-1}}$) assuming CO ($J$:2 → 1)

to CO (J:3 → 2) ratios observed for spiral galaxies (Braine et al. 1993; Mao et al. 2010). Hence, we expect the background CO (J:5 → 4) integrated flux to be $<35.7 \pm 6.1 \, \mathrm{Jy \, km \, s^{-1}}$, which is still consistent with CO (J:5 → 4) being responsible for all the channel flux ($40.0 \pm 5.9 \, \mathrm{Jy \, km \, s^{-1}}$).

Since our ALMA Band 9 observations, targeting CO (J:12 → 11 and J:11 → 10) at $z = 1.027$, were not observed, we defer any study of the CO ladder to a future analysis when more transitions have been observed.

Finally, we highlight the channels with flux levels at the $\sim 2\sigma$ level corresponding to the summed contribution of multiple transitions. At $\sim 242 \, \mathrm{GHz}$, the background CS (J:10 → 9) and [C I $^3P_1 \rightarrow {}^3P_0$] transitions yield together a flux of $14.1 \pm 5.5 \, \mathrm{Jy \, km \, s^{-1}}$. These two transitions were observed by this project, and further discussion is given in Sect. 3.5. At $\sim 270 \, \mathrm{GHz}$, foreground ^{13}CO (J:3 → 2) and $C^{18}O$ (3 → 2) transitions couple with the background $C^{18}O$ (5 → 4) transition, yielding a flux of $8.8 \pm 4.2 \, \mathrm{Jy \, km \, s^{-1}}$. Also, two absorption features may be observed at $\sim 265 \, \mathrm{GHz}$ and $\sim 300 \, \mathrm{GHz}$ (at $\sim 2\sigma$). These frequencies match, among others, those of foreground H_2O, HCO, NH_3, and CH_3OH transitions. Future observations will test the reality of these absorption features.

3.4. CARMA

The system was not spatially resolved by our CARMA observations. The CO (J:2−1) line is offset from the initial tuning, implying an improved redshift estimate (in comparison to that obtained from Z-SPEC) of $z = 1.0271 \pm 0.0002$. The velocity-integrated line flux is $14.4 \pm 1.8 \, \mathrm{Jy \, km \, s^{-1}}$.

3.5. ALMA: line emission

Figure 4 shows the moment maps of the four lines observed with ALMA: CO(2 → 1), CO(4 → 3), [C I $^3P_1 \rightarrow {}^3P_0$] and CS(10 → 9). Each row shows the moment maps of a single spectral line, while each column shows different moments (left to right): integrated spectral line flux (moment 0, M0), velocity field (moment 1, M1), and velocity dispersion (moment 2, M2). The overall Einstein ring morphology is seen in the higher-frequency lines, and the emission can be separated into three main components: the brightest region in the south (knots A+B) is extended towards the north-west (knot D), while a third component is observed in the north-east (knot C). The CO(2 → 1) emission is close to unresolved, but the clean component map shows the presence of the A+B and C knots. All emission lines are detected in the brightest southern component. The CS(10 → 9) line, however, is not reliably detected towards the C and D knots.

The line profiles are also shown in the right-hand column in Fig. 4. The CO shows a double-peaked or plateau profile with a redshifted tail. That is also observed individually in the A+B knot (Fig. 5). Although it is difficult to claim the same for C I and CS, the peaks in the latter do appear to align with those of CO. The line emission from knot D is predominantly observed systematically redshifted.

Table 1 details the emission line parameters for the system as a whole and for each knot. Line luminosities of a transition (L'_{trans}) are estimated as follows:

$$L'_{\text{trans}} = 3.25 \times 10^7 \, S_{\text{trans}} \, \Delta V \, \nu_{\text{obs}}^{-2} \, D_L^2 \, (1 + z)^{-3},$$
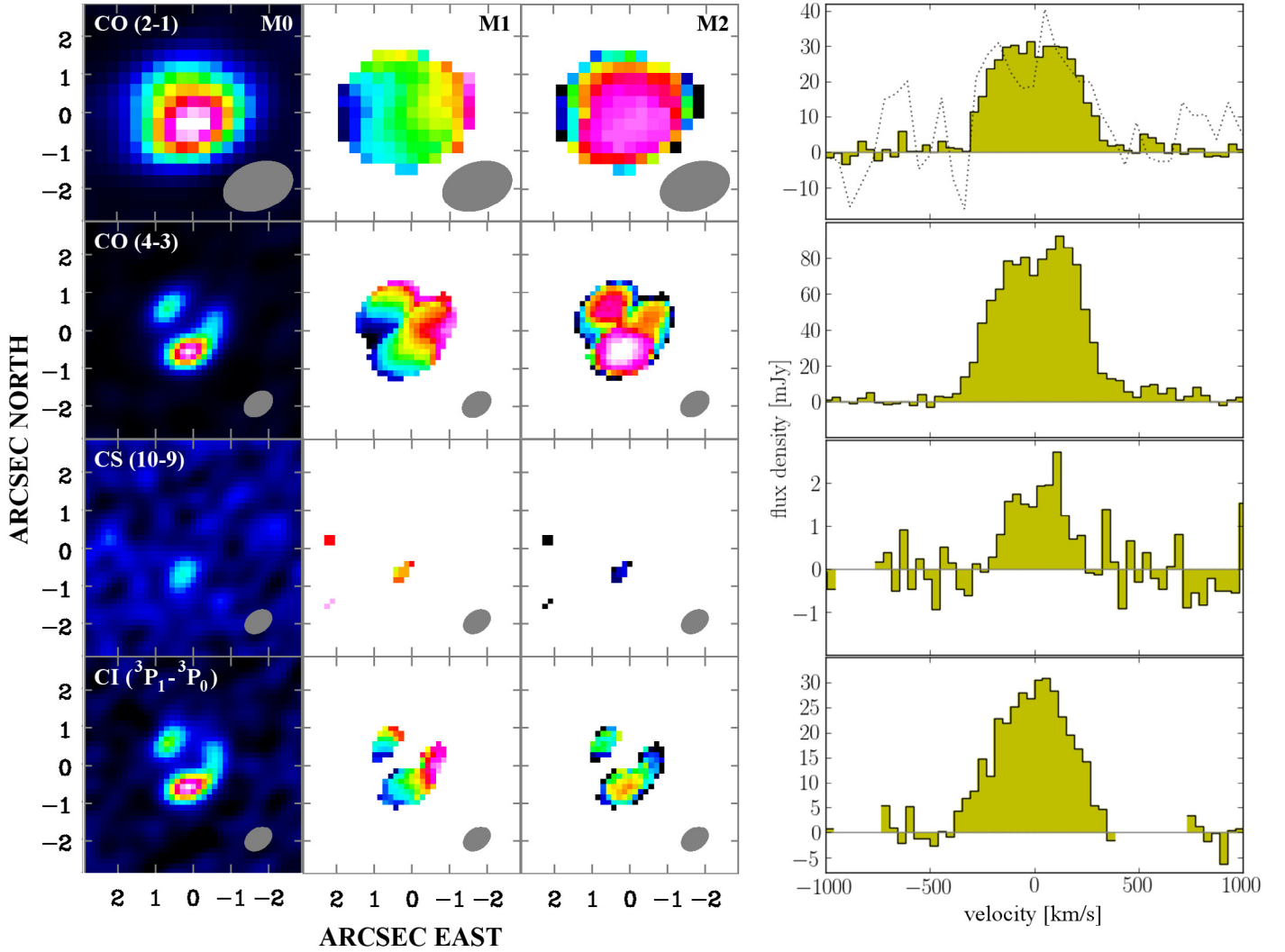
Fig. 4. Moment maps and line profiles of the emission lines detected in H1429−0028 as observed by ALMA: CO(2 → 1) on the *first* (*upper*) *row*; CO(4 → 3) on the *second row*; CS(10 → 9) on the *third row*; [CI ^{3}P$_1$ → ^{3}P$_0$] on the *fourth row*. The columns show different image moments: moment 0 (M0, velocity-integrated flux, *left*), 1 (M1, velocity map, *middle*), and 2 (M2, dispersion map, *right*). Natural weighting was adopted to produce the moments. The beam is shown at the lower right in each panel as a shaded ellipse. Axes units are arcseconds. Colour scales of M0 are from −0.3 to 8 (*first row*), 18 (*second*), 2 (*third*), 5 Jy km s^{-1} (*fourth*). Colour scales in M1 and M2 are, respectively, −200 to 200 km s^{-1} and 0 to 170 km s^{-1}. The *right-most column* shows the line-profiles at a spectral resolution of 40 km s^{-1}. The *first row* also shows the CARMA spectrum as a dotted line.

measured in K km s^{-1} pc^2, where the integrated flux $S_{\text{trans}}\Delta V$ is in Jy km s^{-1}, the observed frequency ν_{obs} is in GHz, and the luminosity distance D_L is in Mpc (e.g., Solomon et al. 1997).

We would like to highlight the flux density agreement between ALMA observations and those of Z-SPEC and CARMA. For instance, even the faint detection of the joint emission from C I ^{3}P$_1$ → ^{3}P$_0$ and CS(10 → 9) in the Z-SPEC spectrum yields a flux estimate (14.1 ± 5.5 Jy km s^{-1}) in good agreement with what is estimated from the ALMA observations (14.2 ± 2.0 Jy km s^{-1}).

As mentioned before, the Z-Spec data suggest an upper limit on CO(5 → 4) luminosity of $L'_{\text{trans}} < 8.04^{+1.37}$. Together with the other observed lines, this yields line ratios of $\frac{L'_{\text{CO(2→1)}}}{L'_{\text{CO(4→3)}}} = 1.37 \pm 0.15$, $\frac{L'_{\text{CO(2→1)}}}{L'_{\text{CO(5→4)}}} > 2.5_{-1.5}$, and $\frac{L'_{\text{CO(4→3)}}}{L'_{\text{CO(5→4)}}} > 1.77_{-0.39}$. Hence, H1429−0028 has values consistent with line ratios observed in SMGs and QSOs (within the natural scatter of these populations, Carilli & Walter 2013).

3.6. ALMA: continuum emission

Continuum-only images were made individually for each spectral window (in each band) after discarding channels with line emission from the transitions presented above. In addition, we then created a higher signal-to-noise continuum map by combining all line-free channels to obtain effective bandwidths of 5.0 GHz and 4.7 GHz in bands 3 and 6, respectively. It should be noted that two of the spectral windows were positioned in the lower side band, and the other two in the upper side band, meaning a frequency gap of 8.2 and 10.4 GHz in bands 3 and 6, respectively.

Table 2 lists the total and knot continuum flux densities in each spectral window and each band. The total flux estimates yield a millimetre spectral index (where $f \propto \nu^{\beta}$) of $\beta = 3.29 \pm 0.40$.

The number of channels used in SPW0 of the band-6 observations (B6-0) is reduced due to atmospheric line flagging, resulting in a larger flux error. In band 3 SPW0 (B3-0), the rms

Table 1. Observed lines in H1429−0028.

Line	Region	Obs. (rest) freq.[a] [GHz]	Redshift	Line peak [mJy]	Integ. flux [Jy km s^{-1}]	Line FWHM[a] [km s^{-1}]	L'_{trans}[b] [1E10 K km s^{-1} pc^2]
CO (J:2 → 1)	Total	113.733 ± 0.001	1.027011 ± 1.8E-5	32.0 ± 6.2	15.1 ± 1.0	469 ± 12	21.2 ± 1.4
	A+B	(230.538)		18.1 ± 3.4	7.98 ± 0.43	507 ± 16	11.22 ± 0.60
	C			10.2 ± 2.0	3.58 ± 0.37	406 ± 17	5.04 ± 0.52
	D			4.5 ± 2.1	1.61 ± 0.35	461 ± 36	2.26 ± 0.49
CO (J:4 → 3)	Total	227.433 ± 0.004	1.027151 ± 3.5E-5	89.9 ± 9.9	43.9 ± 3.7	481 ± 13	15.5 ± 1.3
	A+B	(461.041)		46.1 ± 4.6	24.4 ± 1.9	496 ± 13	8.60 ± 0.65
	C			21.8 ± 4.2	10.2 ± 1.7	445 ± 18	3.57 ± 0.60
	D			17.5 ± 3.8	6.0 ± 1.4	383 ± 19	2.09 ± 0.50
CS (J:10 → 9)	Total	241.568 ± 0.027	1.02738 ± 2.2E-4	3.0 ± 3.2	0.73 ± 0.53	347 ± 83	0.23 ± 0.17
	A+B	(489.751)		3.2 ± 2.6	0.79 ± 0.46	347 ± 83	0.25 ± 0.14
	C			<2.1	−	−	−
	D			<2.1	−	−	−
CI (^{3}P$_1$ → ^{3}P$_0$)	Total	242.819 ± 0.010	1.027181 ± 7.2E-5	33.5 ± 9.6	13.4 ± 2.0	479 ± 27	4.14 ± 0.60
	A+B	(492.161)		18.0 ± 5.4	7.5 ± 1.1	447 ± 21	2.32 ± 0.34
	C			8.9 ± 5.3	3.25 ± 0.89	455 ± 36	1.00 ± 0.27
	D			7.2 ± 3.4	2.38 ± 0.92	404 ± 39	0.73 ± 0.28

Notes. Information of the different line transitions targeted by our ALMA observations. Errors in Cols. 4 to 8 indicate the 1σ uncertainty. Upper limits are set at the 3σ level. Fluxes measured in the clean component map using natural weighting. [a] The observed frequency as computed assuming a Gaussian profile. The value in parenthesis refers to the rest-frame line frequency. [b] The adopted redshift is $z = 1.027$ ($D_{\text{L}} = 6828.3$ Mpc).
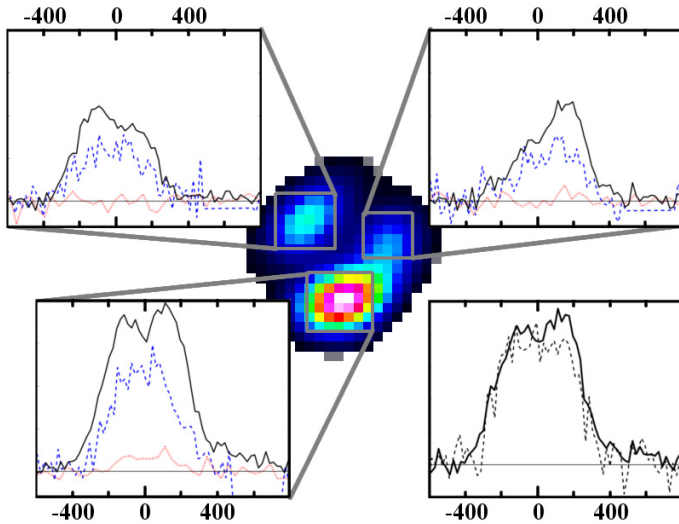

Fig. 5. Line profiles of the emission lines detected in H1429−0028 on each of the specified knots A+B, C and D (grey boxes): CO(4 → 3) as solid black line; CS(10 → 9) as a dotted red line (scaled up by a factor of 2); and [CI ^{3}P$_1$ → ^{3}P$_0$] as dashed blue line (scaled up by a factor of 2). The *bottom right panel* compares the line profiles of the overall CO(2 → 1) (dashed line, scaled up by a factor of 2.5) and CO(4 → 3) (solid line) emission. Different spectral resolutions are considered (20 km s^{-1} for CO(2 → 1), CO(4 → 3) and C I, and 40 km s^{-1} for CS(10 → 9)). The y-axes have the same span in all panels, except the bottom right one. The x-axis range is −600 to 800 km s^{-1} in all panels. The horizontal solid line indicates the zero-flux level. The background colour image is the CO(4 → 3) moment-0 map from Fig. 4.

level is high due to the reduced number of line-free channels in this spectral window targeting CO(2 → 1). As a result, while computing the millimetre spectral index (where $f \propto \nu^\beta$) we adopt the flux density obtained for band-6 SPW1 to compare with that for band 3 SPW1. Such comparison implies a spectral index of $\beta = 3.35 \pm 0.84$. Comparing the *Herschel* 500 μm flux (227 ± 8 mJy) with that at 1.28 mm, one obtains a spectral index of $\beta = 3.89 \pm 0.41$ (having factoring in a conservative 10%

flux calibration uncertainty for *Herschel*). The difference in the slopes, even though consistent within the errors, is expected to result from free-free emission contributing to the 2.8-mm continuum (e.g. Thomson et al. 2012).

3.7. Multi-wavelength photometry

Photometry was gathered in a larger range of the spectrum (from U to 4 cm). The system is of course composed of both the foreground and background galaxies, which contribute differently in each spectral regime. A detailed study of the foreground and background SEDs contribution to the total SED is presented in Sect. 4.2.

The SDSS fluxes refer to the "model magnitudes"[7] provided in the SDSS-DR9 Explore Home (Ahn et al. 2012). This is what is suggested by the SDSS team when the goal is to estimate galaxy colours[8] as it is done in Sect. 4.2. The HST-$F110W$ flux is that within the elliptical aperture used for the deblending analysis described two paragraphs below. The VIKING, *Spitzer* IRAC, and WISE fluxes are measured within a ~8″ diameter aperture. The adopted aperture size does not include neighbour flux given that the closest sources are at a projected distance of ~12″ (very faint source) and ~17″.

Finally, given the angular size of H1429−0028 being much smaller than the FWHM of the *Herschel* bands, *Herschel* SPIRE flux densities are those directly derived by the Multiband Algorithm for source eXtraction (MADX, Maddox et al., in prep.), while *Herschel* PACS flux densities are estimated for the SPIRE source position within apertures of 10″ (100 μm) and 15″ (160 μm). This procedure is described in detail in Rigby et al. (2011). PACS and SPIRE data reduction are described, respectively, in Ibar et al. (2010a) and Pascale et al. (2011).

---

[7] The SDSS magnitudes u and z have been converted to AB magnitudes by adding, respectively, −0.04 and 0.02. The gri photometry is expected to be close to AB. See: http://www.sdss.org/dr5/algorithms/fluxcal.html

[8] http://www.sdss.org/dr7/algorithms/photometry.html

Table 2. Continuum emission from H1429−0028.

SPW	λ_{cent} [mm]	rms [mJy]	Total [mJy]	A+B [mJy]	C [mJy]	D [mJy]
B3[a]	2.80	0.025	0.54 ± 0.11[b]	0.374 ± 0.044	0.107 ± 0.044	<0.075
B3-0	2.64	0.063	0.72 ± 0.22	0.49 ± 0.13	0.20 ± 0.16	<0.19
B3-1	2.67	0.038	0.47 ± 0.13	0.309 ± 0.067	0.058 ± 0.067	<0.11
B3-2	2.94	0.070	0.22 ± 0.10	0.22 ± 0.10	<0.21	<0.21
B3-3	2.97	0.054	0.56 ± 0.16	0.38 ± 0.11	0.111 ± 0.094	<0.16
B6	1.28	0.078	5.86 ± 0.99[b]	3.69 ± 0.28	1.31 ± 0.27	0.71 ± 0.16
B6-0	1.23	0.217	7.1 ± 1.3	4.12 ± 0.86	1.40 ± 0.69	0.79 ± 0.47
B6-1	1.24	0.137	6.15 ± 0.83	3.67 ± 0.48	1.39 ± 0.50	0.76 ± 0.31
B6-2	1.32	0.132	6.12 ± 0.74	3.92 ± 0.48	1.17 ± 0.42	0.95 ± 0.30
B6-3	1.33	0.115	5.29 ± 0.57	3.26 ± 0.40	1.22 ± 0.28	0.50 ± 0.16

Notes. Information of the different continuum bands targeted by our ALMA observations. Numbers in parenthesis indicate the 1σ uncertainty. Upper limits are set at the 3σ level. Flux densities measured in the clean component map using natural weighting. [a] Considering only the line-free spectral windows 1, 2 and 3. [b] The errors consider a conservative 15% error, added in quadrature, to account for flux density calibration uncertainty, as suggested by ALMA staff.

Judging from Fig. 1, the foreground and background sources are more similar in brightness at rest-frame optical than at long wavelengths, where the background emission dominates. In order to estimate the flux of each of the two sources in the high-resolution rest-frame optical imaging (i.e. in the HST *F*110*W* and Keck-AO *H* and K_s band observations), we have used GAL-FIT[9] (version 3.0.4, Peng et al. 2010) to fit and estimate foreground and background fluxes. We have masked out the image pixels dominated by background emission (green contours in left hand-side panels in Fig. 6). The disk galaxy light-profile is considered to be composed of an edge-on disk profile plus a Sérsic index profile (the latter is used to fit the bulge component). Even though the residuals (right hand-side panels in Fig. 6) show over-subtracted regions (likely induced by the dust lane in the foreground galaxy, Fig. 1), we expect this not to be relevant to our analysis, as these regions can be masked out while estimating the background flux (solid white boxes and ellipse in right hand-side panels). Finally, comparing "original" against "foreground-removed" imaging, we estimate background-to-total flux density fraction within the same aperture (red dashed ellipse in the figure). These fractions are $20.9 \pm 1.3\%$ at $1.1\,\mu$m (*F*110*W*), $29.7 \pm 0.1\%$ at $1.6\,\mu$m (*H*-band), and $40.8 \pm 0.1\%$ at $2.2\,\mu$m (K_s-band).

4. Discussion

4.1. Lens model

As referred to in Sect. 3.1, despite presenting a quad-lens-like knot positioning in K_s-band, the relative brightness of the knots is troublesome. While in the rest-frame optical the C knot appears much brighter than the A+B knots, the opposite happens in the CO and mm-to-radio continuum emission (Fig. 1 and Table 1). A few relevant scenarios may explain such multi-wavelength relative knot brightnesses: (i) the background source is extended or clumpy; (ii) significant foreground obscuration is affecting the emission of knots A, B, and D at rest-frame optical wavelengths; (iii) C is being micro-lensed; (iv) a non-standard dark-matter halo structure; (v) variability.

For the current discussion, we will assume that scenarios (iii) and (iv) do not apply given the lack of data to address such possibilities, but we acknowledge their likelihood. Based on the fact

---

[9] http://users.obs.carnegiescience.edu/peng/work/galfit/galfit.html

that the JVLA observations in 2011 June and those of ALMA between 2012 April and July show similar morphology (A+B knot being the brightest), which is distinct from the *F*110*W*-to-K_s imaging (C knot being the brightest) taken between 2011 December and 2012 February, we can safely assume variability is not responsible for the discrepant multi-wavelength morphology. Consequently, scenarios (i) and (ii) are those addressed henceforth.

4.1.1. Lens characterisation

Our analysis is done with the enhanced version of the semi-linear inversion (SLI) method algorithm originally derived by Warren & Dye (2003) and described in Dye et al. (2014). This code does not assume any a priori background morphology and allows multiple datasets to be simultaneously reconstructed using the same lens mass model. Given the likelihood of foreground obscuration at rest-frame optical wavelengths, the images given as input are the velocity-integrated CO(4 → 3) line map and the 7-GHz continuum map. Both maps were reconstructed with similar beam sizes and equal pixel scales.

The lens modelling we pursue assumes an elliptical power-law mass density profile Kassiola & Kovner (1993):

$$\kappa = \kappa_0 (\tilde{r}/1 \text{ kpc})^{1-\alpha}, \qquad (1)$$

where κ is the surface mass density, κ_0 is the normalisation surface mass density, $\tilde{r}$ is the elliptical radius defined by $\tilde{r}^2 = x'^2 + y'^2/\epsilon^2$ (ϵ being the lens elongation defined as the ratio of the semi-major to semi-minor axes), and α is the power-law index relating the volume mass density, ρ, with radius, r: $\rho \propto r^{-\alpha}$. The profile is also described by the orientation of its semi-major axis (θ, measured counter-clockwise from north of the semi-major axis) and the position of the mass centre in the image-plane (x_c, y_c). External shear is not considered, because no evidence of its presence was found during the analysis.

The geometric average of the Einstein radius, θ_E, is computed as

$$\left(\frac{\theta_E}{1 \text{ kpc}} \right) = \left(\frac{2}{3-\alpha} \frac{1}{\sqrt{(\epsilon)}} \frac{\kappa_0}{\Sigma_{\text{CR}}} \right)^{\frac{1}{\alpha-1}}$$

where Σ_{CR} is the critical surface mass density (e.g., Schneider et al. 1992). The best fit parameters resulting from the analysis referred above are $\kappa_0 = 0.399^{+0.005}_{-0.006} \times 10^{10}\ M_\odot$ kpc^{-2},
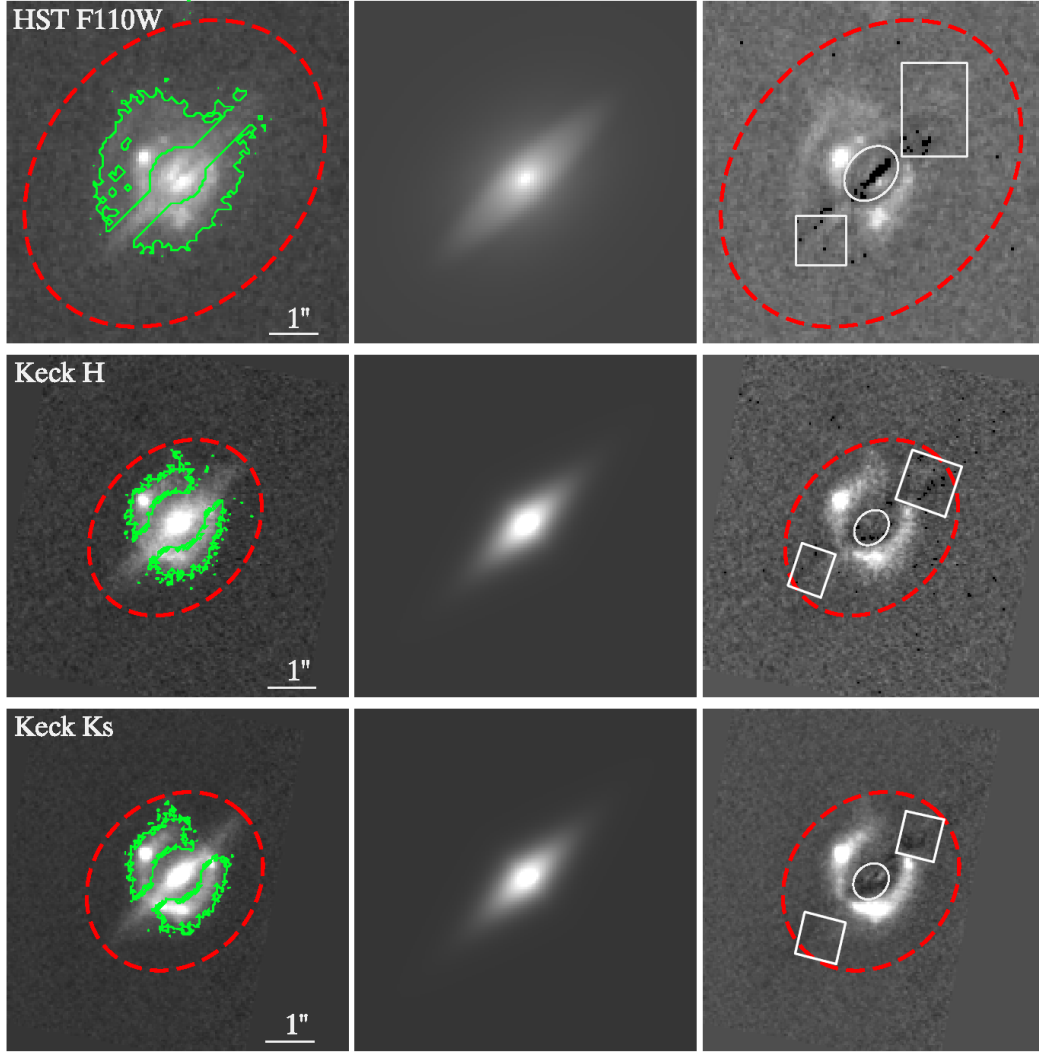
Fig. 6. Using GALFIT to estimate the foreground emission profile. North is up; east is left. *Left-hand side panels* show original imaging from HST *F110W* (*upper row*), Keck-AO *H* (*middle row*), and Keck-AO K_s (*bottom row*). The *right-hand side panels* show the residuals after foreground emission subtraction using the model in the *middle panels*. The green contours in the left panels delimit the mask used to indicate pixels masked out in the GALFIT analysis. The red dashed ellipses encompass the region where the flux was estimated. The extra squared regions on the right panels flag out over-subtracted regions for improved photometry.

$\alpha = 2.08^{+0.07}_{-0.05}$, $\epsilon = 1.46^{+0.04}_{-0.03}$, $\theta = 135.9^{+1.2}_{-1.0}$ deg, and $\theta_E = 2.18^{+0.19}_{-0.27}$ kpc ($0.617^{+0.054}_{-0.075}''$). The confidence limits are shown in Fig. 7.

In order to assess how well each dataset has been reconstructed, we computed (i) the significance (flux density to clean-residual rms ratio) of the flux density in pixels at $>1\sigma$ in the masked residual image; and (ii) the number of residual image pixels with a significance greater than 2.0 as a fraction of the total number of masked image pixels. This is instead of quoting Bayesian evidence, which is meaningless when not comparing models, and is instead of quoting χ^2, which, owing to covariance between the source plane pixels from regularisation in the SLI method, is subject to an ill-defined number of degrees of freedom (ν; see Suyu et al. 2006). Regarding assessment (ii), we measure a fraction of $>2\sigma$ residuals of 0.2% and 0.5% for the 7 GHz and CO ($J{:}4 \rightarrow 3$) data respectively. We have verified that both datasets are well described by Gaussian statistics and therefore attribute the fact that this is significantly lower than the expected fraction of 4.6% to the fact that the SLI method fits away some of the image noise. Assessment (i) yields a residual

flux significance of 1.9 and 0.4 for the 7 Ghz and CO ($J{:}4 \rightarrow 3$) datasets respectively.

An alternative approach to the procedure just presented is described in Calanog et al. (2014), where GALFIT and GRAVLENS (Keeton 2001) are used iteratively to model the lens in the near-IR observed-frame. The surface mass density of the lens is assumed to be described by a singular isothermal ellipsoid (SIE; Kormann et al. 1994). The background source is assumed to comprise one or more components with Sérsic light profiles (Sersic 1968). No foreground obscuration is considered. The best solution implies a complex background morphology (three components) and the following SIE parameters: $b = 0.738^{+0.002}_{-0.001}''$ (the Einstein radius), $\delta x = 0.027^{+0.002}_{-0.002}''$, $\delta y = 0.044^{+0.002}_{-0.003}''$, $\epsilon = 0.208^{+0.005}_{-0.003}$ (the ellipticity), $\theta = -51.0^{+0.5}_{-0.4}$ deg. The fit quality, as assessed via χ^2-statistics, is $\chi^2/\nu = 5452/2097 = 2.6$.

4.1.2. Source-plane reconstruction

The best-fit parameter set was used to also reconstruct the source planes of the 243 GHz, K_s-band, and $F110W$-band continua
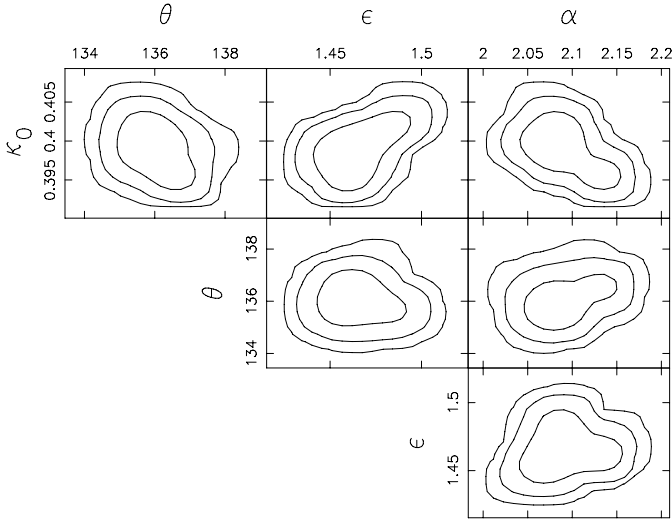
Fig. 7. Parameter confidence space. Parameters shown are the normalisation surface mass density (κ_0 in units of $10^{10}\ M_\odot$ kpc^{-2}), the lens elongation (ϵ), the mass profile power-law index (α), and the orientation of the lens semi-major axis (θ in degrees measured counter-clockwise from north).

emissions. All the reconstructions are shown in Fig. 8. While the 243-GHz continuum map is nicely modelled (no emission peaks above 1.6σ), the algorithm still struggles to fit knot C in the optical rest-frame imaging. This is also reported by Calanog et al. (2014), where even after considering a complex morphology, the fit was still poor. Here, the SLI method analysis is not limited to a priori background morphology and different scenarios of foreground obscuration are considered (based on the GAL-FIT foreground light profile, see Sect. 4.2). Still, the fit is poor. Hence, one concludes that either the foreground obscuration is not properly accounted for (e.g., due to clumpiness), or the surface mass density models adopted in both works fail to explain the background morphology at high spatial resolution ($\lesssim 0.2''$).

The background source morphology at long wavelengths is dominated by extended north-south (NS) emission along the fold and reaching the cusps. There is emission dispersion to the north of the north-west cusp and to the east of the fold. The latter coincides with the dominant emission at rest-frame optical with an approximately east-west (EW) direction. Notice that the NS feature is also observed at rest-frame optical, even though significantly fainter. The two features show a position angle of $\sim 80\deg$[10] between each other and seem to be two distinct components. We take this as evidence of a merger system. Such a scenario may explain the north-eastern arc-like outer feature observed in the $F110W$ band with a length of a few tens of kpc in the source plane (Fig. 9).

In Calanog et al. (2014), the background source is found to be composed of two small sources (effective semi-major axis of $\sim 0.03''$) and a larger ($\sim 0.18''$) third component with a north-south position falling to the east side of the caustic. In terms of surface brightness, the two smaller sources dominate and fall along the position of the EW feature referred to above. Hence, neither approach retrieves an acceptable fit to the near-IR dataset, we consider that the background morphology at those wavelengths is fairly consistent between the two independent results.

---

[10] As observed in K_s-band imaging, where the features appear more clearly.

As for a toy model, we show in Fig. 9 the Antennæ galaxies for comparison. Although it is not a 100% match, the resemblance is significant, explaining properties such as why the optical and mm frames are dominated by different components, and the presence of tidal tails appearing north-eastwards and southwards to the caustic on, respectively, the $F110W$ imaging and the $F110W$ and 7-GHz imaging.

4.1.3. Source dynamical analysis

The dynamical analysis is, at this point, limited to the north-south component. Future optical integral field spectroscopy or deeper ALMA observations are required to study the east-west component. Applying the best-fit lens model to the CO ($J{:}4 \rightarrow 3$) cube allows one to study the source dynamics in the source plane. Figure 10 shows the CO ($J{:}4 \rightarrow 3$) moment maps: velocity-integrated line flux, velocity field, and velocity dispersion. It is clear that the southern emission is predominantly blueshifted, while that in the north is at the systemic redshift ($\Delta v \sim 0\ \mathrm{km\,s^{-1}}$) or redshifted. The largest velocity dispersion is coincident with the emission peak and extending to the north.

In order to estimate the dynamical mass of the background source, we consider the "isotropic virial estimator":

$$M_{\rm dyn} = 2.8 \times 10^5\ (\Delta v_{\rm FWHM})^2\ r_{1/2},$$

where $[M_{\rm dyn}] = M_\odot$, $\Delta v_{\rm FWHM}$ is the CO ($J{:}4 \rightarrow 3$) FWHM ($481 \pm 13\ \mathrm{km\,s^{-1}}$), and $r_{1/2}$ is the half-light radius in units of kpc.

With such disturbed source-plane morphology, we avoid fitting a light-profile (e.g., Sérsic), and adopt an alternative method to estimate $r_{1/2}$. First, the source centre ($x_{\rm c}, y_{\rm c}$) is found by minimising the second-order moment of the source pixels:

$$M_{\rm total} = \sum_i^n f_i\ \left[(x_i - x_{\rm c})^2 + (y_i - y_{\rm c})^2 \right],$$

where f_i, x_i, and y_i are, respectively, the flux and coordinates of each pixel. The half-light radius was then considered to be equal to the maximum extension in respect to the estimated source centre among the pixels comprising half the source flux. The uncertainties were found via bootstrapping, i.e., the pixel flux values were shifted within $\pm$rms, and $r_{1/2}$, $x_{\rm c}$, and $y_{\rm c}$ were recomputed for a total of 10 000 iterations. The estimated half-light radius is found to be $r_{1/2} = 0.90 \pm 0.26\ \mathrm{kpc}$, and the dynamical mass to be $5.8 \pm 1.7 \times 10^{10}\ M_\odot$. The discussion continues in Sect. 4.5, after stellar, dust and inter stellar medium (ISM) gas masses are estimated.

4.1.4. Magnification factor

Table 3 shows the estimated magnifications depending on wavelength and source-plane region. The latter is addressed in the columns $\mu_{\rm TOT}$, μ_{50}, and μ_{10} referring, respectively, to the ratio between the total image flux and the total source-plane flux, and the magnification of the brightest region in the source plane that contains 50% and 10% of the total source-plane flux. Considering these, the spatial differential magnification is clear, with differences of up to a factor of ~ 4. This is unsurprising given the spatial extent of the source and its proximity to the caustic. Hereafter, the adopted value for magnification will be $\mu_{\rm TOT}$. As a comparison, we note that Calanog et al. (2014) estimate a K_s-band magnification factor ($9.6^{+1.0}_{-0.3}$) consistent with the value implied by the analysis presented here (8.9 ± 0.7).
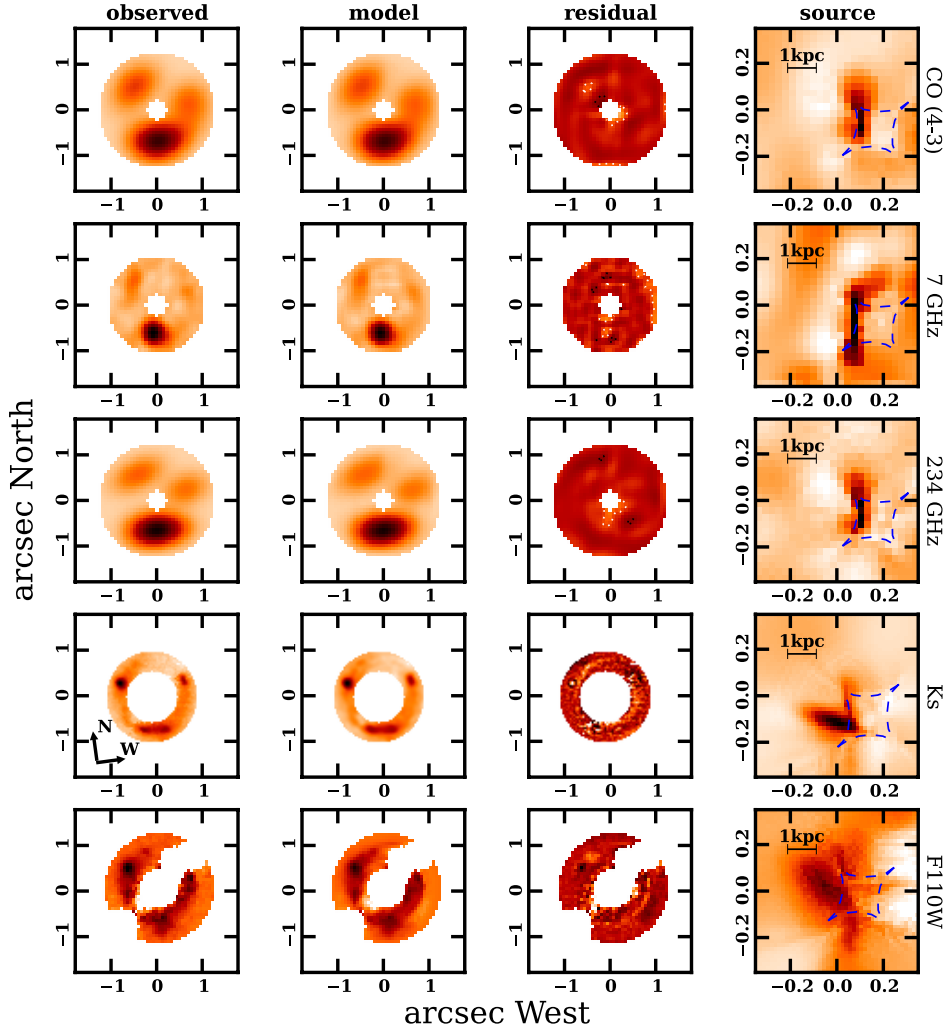
Fig. 8. Multi-wavelength source reconstruction of H1429−0028: CO (J:4 → 3) (uniform weight, *top row*); 7-GHz continuum (Briggs weight, robust = 5, *top middle row*); 234-GHz continuum (uniform weight, *middle row*); K_s-band (*bottom middle row*); and $F110W$-band (*bottom row*). *Left column* shows the observation data, while the *second column* shows the model image-plane. The *third column* shows the residuals with a scale range from −4σ to 4σ. Contours show −3σ (solid white), −1σ (dotted white), 1σ (dotted black), and 3σ (solid black) levels. The *fourth column* shows the source-plane reconstruction, with the caustic overlaid, and the physical scale given by the errorbar. The K_s-band frames have a slight tilt shown by the two arrows in the *left column*.

4.1.5. Stellar mass contribution to the lens effect

In Sect. 4.2 we estimate the foreground stellar mass to be $2.8^{+2.0}_{-1.2} \times 10^{10} M_\odot$. Adopting the fraction of light in the K_s band within the average Einstein radius (57%) to be a proxy of the fraction of the stellar mass within that same radius ($1.60^{+1.1}_{-0.69} \times 10^{10} M_\odot$), one can estimate the stellar mass contribution to the lens effect. From the lens analysis and integrating Eq. (1) over theta and radius, we know that the total mass within the average Einstein radius is $M(<\theta_E) = 8.13^{+0.33}_{-0.41} \times 10^{10} M_\odot$. Hence, the stellar mass contribution to the deflection effect is $19.7^{+14}_{-8.5}$%.

4.2. Foreground and background SEDs

As expected for a GL system such as H1429−0028, the SED is actually a combination of two individual SEDs, and their de-blending is required to study each galaxy separately. The spatially resolved photometry of the two galaxies in the $F110W$, H, and K_s bands, and ALMA observations indicate that, down to the data sensitivity, the background system is the sole contributor at least in the mm spectral range. Given the lack of

spatially resolved photometry, we avoid working with best-fit solutions and consider instead flux probability distribution functions (PDFs). To obtain these, we utilise the MAGPHYS[11] software (da Cunha et al. 2008). This code considers the latest version of the Bruzual & Charlot (2003) stellar population synthesis code, where the new prescription by Marigo & Girardi (2007) for the thermally pulsating asymptotic giant branch evolution of low- and intermediate-mass stars is considered.

We first remove foreground light from the total SED. The foreground rest-frame optical spectral range is traced by the high-resolution imaging in the $F110W$, H, and K_s bands. To help constrain the obscuration at short-wavelengths, we consider a g-band upper-limit 3σ away from the total-flux detection. Also, the non-detection at mm wavelengths provides an upper-limit (at the 3σ level) with which to better constrain that region of the foreground SED. In order to take into account errors in the multi-waveband analysis (i.e., mismatched aperture sizes and absolute zero points, and calibration errors), we add in quadrature 0.1 mag (~9% of the flux) to the photometric error. The foreground redshift is fixed at $z = 0.218$, and the redshift uncertainty
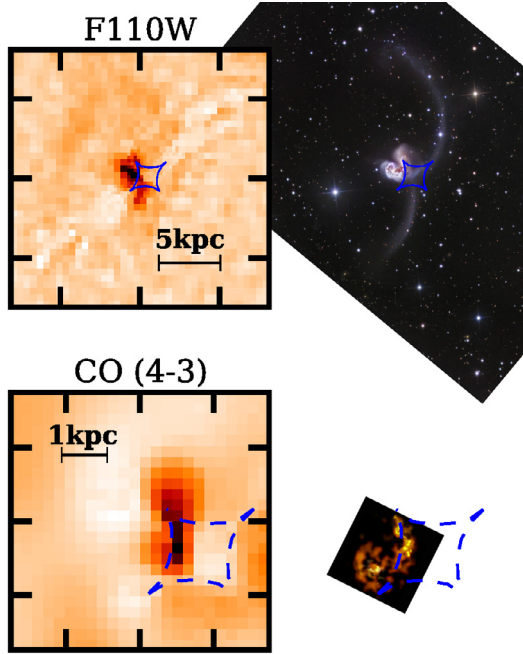
---

[11] http://www.iap.fr/magphys

Fig. 9. Using the Antennæ galaxy merger as a toy model to help visualise the background galaxy of H1429-0028. The *two upper images* show the *F110W* source-plane reconstruction from Fig. 8 (left hand-side) and the Antennæ galaxies as seen in the optical (right hand-side). The *two bottom images* show the CO (J:4 → 3) velocity-integrated flux source-plane reconstruction from Fig. 8 (left hand-side) and the CO (J:J^{up} = 1, 2, 3) map in the Antennæ galaxies as observed by ALMA. Image credits: NASA, ESA and Ivo Saviane (*upper-right picture*), ALMA (ESO, NRAO, NJAO; *bottom-right picture*).

Table 3. Multi-wavelength magnification of H1429−0028.

Data	$\mu_{\mathrm{TOT}}{}^a$	$\mu_{50}{}^b$	$\mu_{10}{}^c$
HST *F110W*	7.9 ± 0.8	11.0 ± 0.9	7.3 ± 0.9
Keck K_{s}	8.9 ± 0.7	11.0 ± 0.7	11.2 ± 0.7
ALMA CO (J:4 → 3)	9.7 ± 0.7	13.9 ± 0.9	25.0 ± 1.9
ALMA 234 GHz	10.8 ± 0.7	14.3 ± 0.8	26.0 ± 2.0
JVLA 7 GHz	5.2 ± 0.5	11.6 ± 1.1	20.2 ± 1.8

Notes. [a] The ratio between the total image flux and the total source-plane flux. [b] The magnification of the brightest region in the source plane that contains 50% of the total source-plane flux. [c] The magnification of the brightest region in the source plane that contains 10% of the total source-plane flux.

SED, which yields $\tau_V = 3.39^{+0.86}_{-0.96}$. The assumed background morphology is that observed in the Keck AO K_{s}-band. The final adopted flux estimate is the average between the maximum and minimum values (including error) from the three scenarios, with an error equal to the maximum deviation from the average.

The "continuum" data point from MAMBO2 was left out from the analysis due to line contamination. Considering the MAMBO2 response curve[13], the ALMA estimates for the continuum level, line-flux estimates for CO(4 → 3) and C I(^{3}P$_1$ →^{3} P$_0$), and Z-SPEC for CO(5 → 4), and a spectral slope $\alpha = 3.89 \pm 0.09$ (Sect. 3.6), one should observe a MAMBO2 flux of ∼10.0 ± 0.14 mJy, which is more in agreement with the actual observed value (10.3 ± 2.5 mJy). The ALMA band-3 continuum estimate (rest-frame 216 GHz) was also discarded given the evidence of free-free emission contamination (see also Condon 1992; Thomson et al. 2012; Clemens et al. 2013) during the analysis.

We also attempt to correct for differential magnification by demagnifying the bands shortwards the K_{s}-band (inclusive) by a factor of 8.9 ± 0.7, by 9.85 ± 1.65 the bands shortwards of 1.28 mm (exclusive), and by 10.8 ± 0.7 the 234-GHz continuum flux (Table 3).

Finally, given the nature of the source, the standard models accompanying MAGPHYS have shown limitations to cover the necessary physical parameter space, as described by Rowlands et al. (2014); hence, for the background source, we have adopted the models presented in that same work, which are better suited for more extreme star-forming systems.

Considering the above assumptions, Table 4 shows the observed and model predicted fluxes for both foreground and background systems. For the latter, the predicted fluxes are compared to input flux values (after foreground removal and flux demagnification) in Fig. 11. Table 5 shows the SED fit results of the physical properties for both fore and background SEDs. The PDFs of the background physical parameters are shown in Fig. 12. The ISM dust temperature is poorly constrained, hence not shown.

Although the fit is generally good, there is a slight tension in the 350-μm, 500-μm and 1.28-mm bands. The deviation in the *Herschel* bands may be, respectively, assigned to emission from [C II] and CO (J^{up} = 9−12). For instance, considering the [C II]-to-FIR relation from Díaz-Santos et al. (2013), we estimate a [C II] flux contribution to the 350-μm band of $8.2^{+11.3}_{-4.7}$% (see also Smail et al. 2011). Such an effect, however, does not explain the overestimate at 1.28 mm, even though just at a ∼2σ level.

Hence, we have also considered the algorithm which fits modified black-body models to photometry data

is considered negligible compared to the photometric uncertainties just mentioned. This procedure yields a flux PDF for each band[12]. These PDFs were used to determine the amount of foreground flux to remove from total photometry flux. The difference between the two in each band gives the background flux.

Before one proceeds to analyse the resulting background SED, one has to correct for the possible foreground extinction affecting knots A, B, and D at short wavelengths (Fig. 1). We thus consider three scenarios: (i) there is no foreground extinction; (ii) the extinction is linearly proportional to or (iii) weighted on pixel flux of the foreground light-profile model obtained with GALFIT. The difference between scenarios (ii) and (iii) is that extinction will be more centrally concentrated in (iii). Scenarios (ii) and (iii) can be translated into the following equations:

$$\text{(ii) } e_i^{-\tau_\lambda} = f_i \frac{e^{-\tau_\lambda}}{\overline{f}} \tag{2}$$

$$\text{(iii) } e_i^{-\tau_\lambda} = f_i \frac{e^{-\tau_\lambda}}{\frac{\sum f_i^2}{\sum f_i}} \times \frac{f_i}{\frac{\sum f_i^2}{\sum f_i}} = e - \tau_\lambda \left(\frac{f_i}{\frac{\sum f_i^2}{\sum f_i}} \right)^2 \tag{3}$$

where the i index refers to a given pixel at >3σ, f_i is the pixel flux, $\overline{f}$ and $\frac{\sum f_i^2}{\sum f_i}$ are, respectively, the foreground light-model flux average and weighted average of pixels at >3σ, and τ_λ is the absorption optical depth at a given waveband. The latter is obtained with Eqs. (3) and (4) from da Cunha et al. (2008), where τ_V is given in this work by the MAGPHYS analysis of the foreground

---

[12] The use of upper-limits and the extraction of flux PDF was possible after changing the standard MAGPHYS code publicly available.

[13] http://www.astro.uni-bonn.de/~bertoldi/projects/mambo/manuals.html
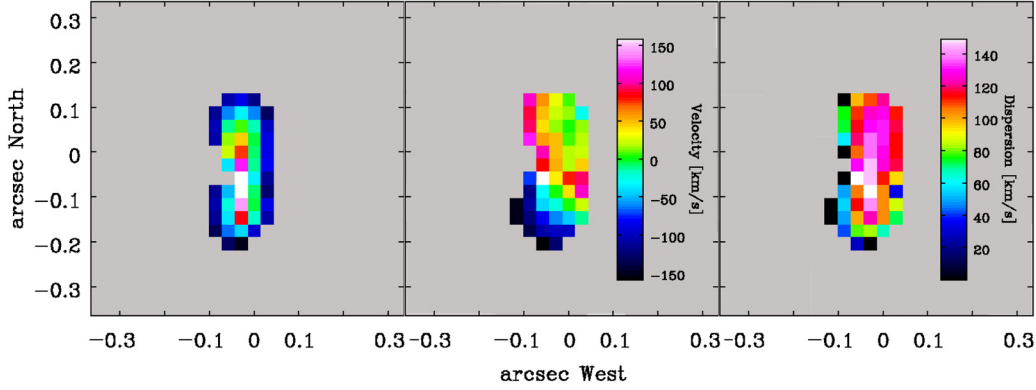
Fig. 10. Source-plane dynamical properties of H1429−0028. The *left hand-side panel* shows the velocity-integrated intensity map. The *middle panel* shows the velocity field, while the *right hand-side panel* shows the velocity dispersion map. Colour scales for the middle and right panels are given by the inset bar.
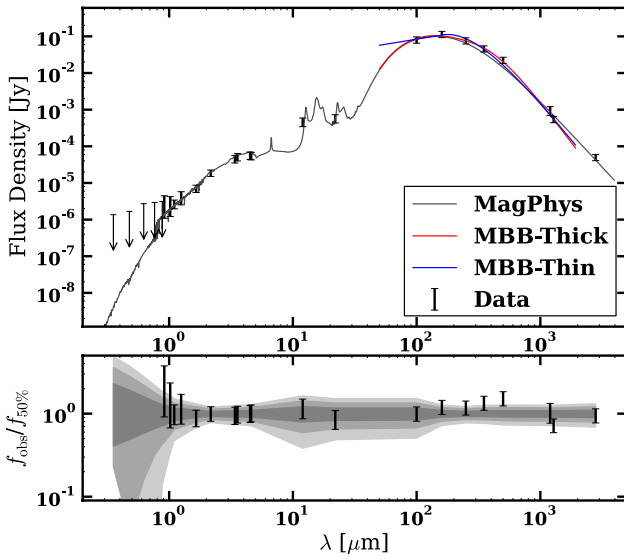

Fig. 11. Comparing the input flux data points (errorbars) and the predicted fluxes by MAGPHYS (grey regions referring to 1σ, 2σ, and 3σ confidence intervals in the *bottom panel*). The best fit model from the MAGPHYS analysis is shown as a grey solid line. The best-fit models from the modified black body fitting are shown as red (optically-thick case) and blue (optically-thin) solid lines. The *bottom panel* shows the flux ratios with respect to the 50% quartile of the flux PDF at a given band.

(MBB_EMCEE[14], see, for instance, Riechers et al. 2013; Fu et al. 2013) using an affine invariant Markov chain Monte Carlo method (Foreman-Mackey et al. 2013). The difference to MAGPHYS is that, although MBB_EMCEE considers only one emission component, the parameter range is not limited to input models and the optically-thick scenario can also be explored. Table 6 summarises the results and Fig. 11 shows the best-fit models. In order to compute these values, it was necessary to limit β below 3, the temperature to observed-frame 100 K, and, in the optically-thick case, λ_0 below observed-frame 2000 μm. While it is not straightforward to compare the success between the two codes based of the χ^2 value (due to the constrain in certain parameters), both scenarios improve the fit to the FIR-to-mm spectral range. Interestingly enough, the dust mass and IR luminosity values are consistent within the errors with those obtained with MAGPHYS.

[14] https://github.com/aconley/mbb_emcee

4.3. Radio-FIR correlation and SFRs

The direct comparison between mm and cm imaging allows us to infer the radiation mechanisms responsible for both emissions. Specifically the ratio between the $8-1000\,\mu$m and 1.4-GHz fluxes, the $q_{\rm TIR}$ parameter, has been frequently used to distinguish star-forming from AGN dominated regions, with a value of 2.64 ± 0.26 being characteristic of local star-forming galaxies with no signs of AGN activity (Bell 2003)[15]. In Bell (2003), this parameter is defined as

$$q_{\rm TIR} = \log_{10}\left(\frac{\rm TIR}{3.75 \times 10^{12}\,{\rm W\,m^{-2}}}\right) - \log_{10}\left(\frac{S_{1.4\,\rm GHz}}{\rm W\,m^{-2}\,Hz^{-1}}\right),$$

where TIR is the total $8-1000\,\mu$m IR flux in W m^{-2}, and $S_{1.4\,\rm GHz}$ is the 1.4-GHz flux density in W m^{-2} Hz^{-1}. We convert the observed 7-GHz flux densities to rest-frame 1.4-GHz flux densities assuming a power-law index of 0.8 ± 0.2 ($f \propto \nu^{-0.8}$) characteristic of synchrotron radiation (e.g., Ibar et al. 2010b; Thomson et al. 2014). We consider the different magnifications of 10.8 ± 0.7 and 5.2 ± 0.5, respectively, for the IR and radio spectral regimes. In H1429−0028, we find $q_{\rm TIR} = 1.9^{+1.1}_{-1.2}$, which is consistent with the value found for normal galaxies within 1σ.

Finally, we estimate IR and radio SFRs by assuming the IR and radio luminosity-to-SFR calibrations proposed by Bell (2003, see also Kennicutt 1998), which account for the contribution from old stellar populations:

$$SFR[M_\odot\,{\rm yr}^{-1}] \equiv \begin{cases} 1.57 \times 10^{-10}\,L_{\rm TIR}\left(1 + \sqrt{10^9/L_{\rm TIR}}\right) \\ 5.52 \times 10^{-22}\,L_{1.4\,\rm GHz} \end{cases} \quad (4)$$

where $[L_{1.4\,\rm GHz}] = {\rm W\,Hz}^{-1}$, $[L_{\rm TIR}] = [L_{8-1000\,\mu m}] = L_\odot$. The intrinsic IR and radio SFRs are estimated to be, respectively, $3.9^{+8.1}_{-2.0} \times 10^2$ and $9.3^{+20}_{-6.5} \times 10^2\,M_\odot\,{\rm yr}^{-1}$, where the error takes into account a factor of 2 due to the expected scatter in the relations (Bell 2003). Within 1σ, these estimates are in agreement with that obtained from the MAGPHYS analysis.

4.4. Molecular gas and ISM gas masses of the background galaxy

As previously mentioned, the available number of CO transitions is not enough to properly constrain the CO ladder, nor do

[15] Yun et al. (2001) define the same parameter with reference to the $42.5-122.5\,\mu$m spectral range. By doing so, normal star-forming galaxies are expected to have $q = 2.34 \pm 0.26$ (Bell 2003).
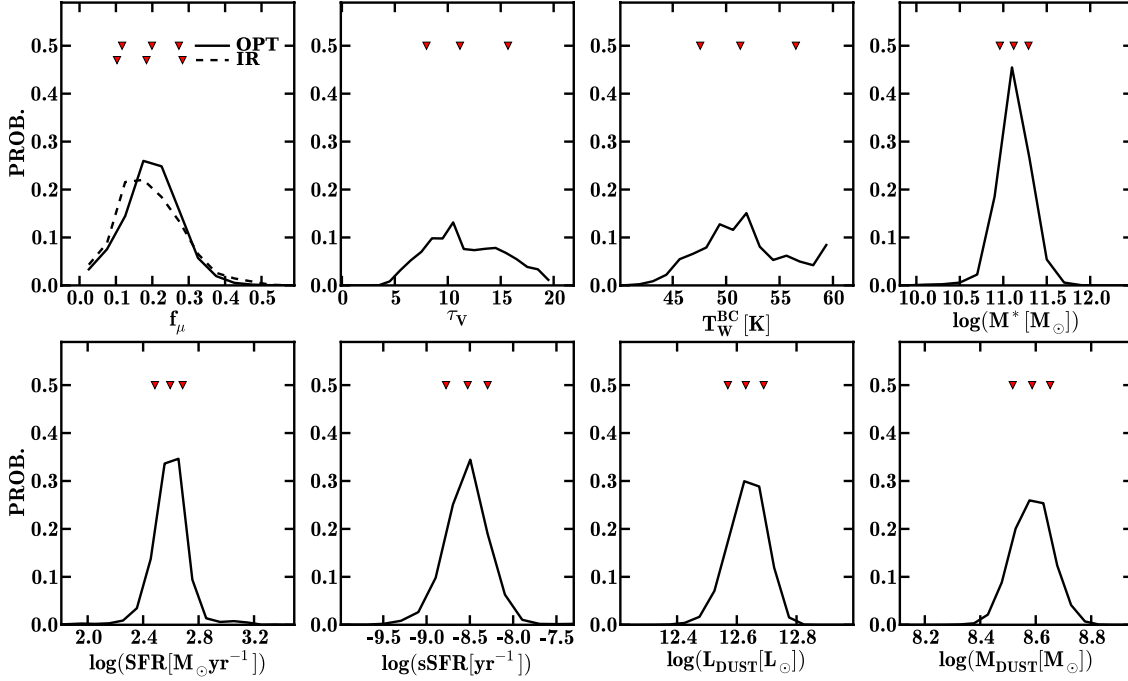
Fig. 12. Background SED fit analysis results. Each panel shows the PDF of a given physical parameter (*top left*: energy fraction absorbed by the ISM as estimated from stellar-dominated, OPT, or dust-dominated photometry, IR; *top middle left*: total effective V-band optical depth seen by stars in birth clouds; *top middle right*: warm dust temperature in birth clouds; *top right*: stellar mass; *bottom left*: star-formation rate; bottom middle-left: specific star-formation rate; *bottom middle right*: dust luminosity; bottom right: dust mass). The red inverted triangles indicate the 16th, 50th, and 84th percentiles.

we have a reliable $\mathrm{CO}\,(J{:}5 \to 4)$ flux measurement. Hence, in order to compute total molecular gas masses, one has to rely on certain assumptions or empirical statistical relations available in the literature.

It is clear from the detection of $\mathrm{CS}\,(J{:}10 \to 9)$ that the observed background $^{12}\mathrm{CO}$ emission is optically-thick. Nevertheless, assuming local thermodynamical equilibrium (LTE) and an optical thin transition, one can estimate a mass lower limit. We assume the nomenclature $X_{\mathrm{CO}}^{\mathrm{thin}} = \frac{M_{\mathrm{H_2}}}{L'_{\mathrm{CO}(J{:}1\to0)}}$, where

$$X_{\mathrm{CO}}^{\mathrm{thin}} \sim 0.08 \left[\frac{g_1}{Z} e^{-T_o/T_k} \left(\frac{J(T_k) - J(T_{\mathrm{bg}})}{J(T_k)} \right) \right]^{-1}$$

$$\times \left(\frac{[\mathrm{CO/H2}]}{10^{-4}} \right)^{-1} \frac{M_\odot}{\mathrm{K\,km\,s^{-1}\,pc^2}},$$

with $T_o = E_u/k_B \sim 5.5\,\mathrm{K}$, $J(T) = T_o(e^{T_o/T} - 1)^{-1}$, $T_{\mathrm{bg}} = (1 + z)T_{\mathrm{CMB}} = 5.524\,\mathrm{K}$ (the temperature of the cosmic microwave background at $z = 1.027$), $g_1 = 3$ (the degeneracy of level $n = 1$), $Z \sim 2T_k/T_o$ (the partition function), T_k is assumed to be equal to that estimated by MBB_EMCEE in the optically-thin case ($35.9^{+4.3}_{-4.3}$ K, Table 6), $[\mathrm{CO/H2}] = 10^{-4}$ (the CO abundance in typical molecular clouds or in a solar-metallicity environment, Bryant & Scoville 1996), and Helium mass is already considered. These assumptions result in $X_{\mathrm{CO}}^{\mathrm{thin}} \sim 0.449^{+0.040}_{-0.039}$. Due to the absence of a $\mathrm{CO}(1 \to 0)$ observation, we base our $\mathrm{CO}\,(J{:}1 \to 0)$ line luminosity in that observed for $\mathrm{CO}\,(J{:}2 \to 1)$ assuming a conversion factor of $L'_{\mathrm{CO}\,2\to1}/0.92$ (Carilli & Walter 2013). This yields a molecular mass lower limit of $M_{\mathrm{H_2}} > 1.03^{+0.11}_{-0.11} \times 10^{11} \mu^{-1} M_\odot$. Following Ivison et al. (2011), an upper limit may be estimated assuming $X_{\mathrm{CO}} = 5$ (observed in giant molecular clouds, Solomon et al. 1987; Solomon & Barrett 1991), which yields $M_{\mathrm{H_2}} < 1.15 \pm 0.08 \times 10^{12} \mu^{-1} M_\odot$. Hence,

based on the $\mathrm{CO}\,(J{:}2 \to 1)$ observations, we expect the intrinsic molecular mass to be in the range $1.07_{-0.14} < M_{\mathrm{H}}2[Mo/1E10] < 11.87^{+1.17}$.

Recently, Narayanan et al. (2012) proposed a simple relation between X_{CO}[16] and CO and metallicity measurements:

$$X_{\mathrm{CO}} = \frac{10.7 \times \langle W_{\mathrm{CO}} \rangle^{-0.32}}{Z'^{0.65}},$$

where $\langle W_{\mathrm{CO}} \rangle$ is the luminosity-weighted CO intensity, measured in $\mathrm{K\,km\,s^{-1}}$, and Z' is the metallicity divided by the Solar metallicity. Assuming $Z' = 0.50^{+0.50}_{-0.25}$, the relation yields $X_{\mathrm{CO}} = 6.6^{+2.2}_{-4.3}$. The errors are still consistent with the range we adopted previously. However, either assumption implies a large range of $M_{\mathrm{H_2}}$.

An alternative to using CO emission to estimate $M_{\mathrm{H_2}}$ is to use the forbidden fine-structure transitions of neutral carbon ([C I]). The critical density of both [C I] and $^{12}\mathrm{CO}$ are $n \sim 10^3\,\mathrm{cm^{-3}}$. Also, [C I] traces only molecular gas, as a result of being insensitive to the presence of atomic or ionised gas. However, here too, one must assume an optically thin [C I] line in LTE in order to estimate [C I] masses as

$$M_{\mathrm{C\,I}} = 5.706 \times 10^{-4} Q(T_{\mathrm{ex}}) \frac{1}{3} e^{23.6/T_{\mathrm{ex}}} L'_{\mathrm{C\,I}(^3P_1 \to {}^3P_0)}$$

where $[M_{\mathrm{C\,I}}] = M_\odot$, $[L'_{\mathrm{C\,I}(^3P_1 \to {}^3P_0)}] = \mathrm{K\,km\,s^{-1}\,pc^2}$, and $Q(T_{\mathrm{ex}}) = 1 + 3e^{-T_1/T_{\mathrm{ex}}} + 5e^{-T_2/T_{\mathrm{ex}}}$ is the [C I] partition function, with $T_1 = 23.6\,\mathrm{K}$ and $T_2 = 62.5\,\mathrm{K}$ being the energies above the ground state for the [C I($^3P_1 \to {}^3P_0$)] and [C I($^3P_2 \to {}^3P_1$)] lines, respectively. The [C I($^3P_2 \to {}^3P_1$)] line, however, is redshifted

---

[16] The nomenclature for X_{CO} we adopt here is that adopted in Narayanan et al. (2012) for α_{CO}.

Table 4. Multi-wavelength photometry of H1429−0028.

Survey/ facility	Filter	Total [μJy]	Foreg. [μJy]	Backg.[a] [μJy]
SDSS	u	<4.9	$0.80^{+0.95}_{-0.45}$	$0.004^{+0.006}_{-0.003}$
	g	5.9 ± 0.8	$4.3^{+2.7}_{-1.7}$	$0.024^{+0.022}_{-0.012}$
	r	20.5 ± 1.1	$15.1^{+5.1}_{-4.0}$	$0.11^{+0.07}_{-0.05}$
	i	35.3 ± 1.9	$26.8^{+5.7}_{-5.0}$	$0.38^{+0.15}_{-0.13}$
	z	61.9 ± 7.4	$42.4^{+5.9}_{-5.6}$	$1.19^{+0.33}_{-0.33}$
VIKING	Z	52.7 ± 3.1	$40.7^{+5.9}_{-5.6}$	$1.11^{+0.32}_{-0.32}$
	Y	78.8 ± 5.9	$59.0^{+6.1}_{-6.1}$	$1.80^{+0.40}_{-0.40}$
	J	133.9 ± 6.7	$102.1^{+4.1}_{-4.8}$	$3.4^{+0.5}_{-0.5}$
	H	192 ± 12	134.8 ± 8.4	6.4 ± 0.6[b]
	K_s	380 ± 12	224.7 ± 6.9	17.4 ± 1.5[b]
HST	$F110W$	98.8 ± 4.2	78.1 ± 3.5	2.6 ± 0.3[b]

Survey/ facility	Filter	Total [mJy]	Foreg. [mJy]	Backg. [mJy]
Spitzer	$3.6\,\mu$m	0.614 ± 0.003	$0.130^{+0.031}_{-0.023}$	$0.052^{+0.004}_{-0.005}$
	$4.5\,\mu$m	0.673 ± 0.004	$0.136^{+0.042}_{-0.029}$	$0.056^{+0.005}_{-0.005}$
WISE	$3.4\,\mu$m	0.558 ± 0.014	$0.131^{+0.029}_{-0.022}$	$0.047^{+0.004}_{-0.004}$
	$4.6\,\mu$m	0.653 ± 0.020	$0.130^{+0.038}_{-0.028}$	$0.053^{+0.005}_{-0.005}$
	$12\,\mu$m	5.39 ± 0.15	$0.78^{+0.84}_{-0.48}$	$0.40^{+0.08}_{-0.08}$
	$22\,\mu$m	6.22 ± 0.76	$0.51^{+0.59}_{-0.31}$	$0.67^{+0.12}_{-0.11}$
Herschel	$100\,\mu$m	821 ± 28	23^{+20}_{-12}	80^{+14}_{-13}
	$160\,\mu$m	1164 ± 32	33^{+23}_{-15}	$94.8^{+8.7}_{-8.9}$
	$250\,\mu$m	778 ± 6	23^{+15}_{-10}	$64.4^{+4.6}_{-4.9}$
	$350\,\mu$m	467.0 ± 7.0	$11.4^{+7.7}_{-5.3}$	$34.0^{+2.9}_{-2.7}$
	$500\,\mu$m	227.0 ± 8.0	$4.6^{+3.2}_{-2.2}$	$14.7^{+1.3}_{-1.3}$
IRAM-30	1.2 mm	10.3 ± 2.5	$0.23^{+0.18}_{-0.11}$	$0.910^{+0.081}_{-0.086}$
ALMA	1.28 mm	5.86 ± 0.99	$0.18^{+0.15}_{-0.09}$	0.543 ± 0.098[c]
	2.8 mm	0.54 ± 0.11	$0.0014^{+0.0011}_{-0.0007}$	$0.0525^{+0.0056}_{-0.0055}$
JVLA	7 GHz	0.91 ± 0.08	<0.03	0.175 ± 0.023[c]

Notes. Upper limits are set at the 3σ level. [a] Intrinsic (demagnified) fluxes. [b] Estimated via direct analysis of high-resolution HST *F110W*, Keck AO H and K_s imaging and demagnified by $\mu = 7.9 \pm 0.8$ in the former and $\mu = 8.9 \pm 0.7$ in the Keck bands. [c] Assumed to be equal to the total flux and demagnified by $\mu = 10.8 \pm 2$ at 1.28 mm and $\mu = 5.2 \pm 0.5$ at 7 GHz (Table 3).

Table 5. MAGPHYS SED analysis.

Source	f_μ (SFH/IR)[a]	τ_V	T^{ISM} [K]	T^{BC} [K]	M^* [$10^{10}\,M_\odot$]	SFR [$M_\odot$ yr^{-1}]	sSFR [10^{-10} yr^{-1}]	L_{dust} [$10^{11}\,L_\odot$]	M_{dust} [$10^8\,M_\odot$]
Foreg.	$0.81^{+0.14}_{-0.18}$ $0.79^{+0.13}_{-0.19}$	$3.39^{+0.86}_{-0.96}$	$22.1^{+2.1}_{-3.0}$	$45.5^{+9.8}_{-10}$	$2.8^{+2.0}_{-1.2}$	$1.2^{+2.5}_{-0.9}$	$0.43^{+1.3}_{-0.36}$	$0.44^{+0.34}_{-0.21}$	$0.44^{+0.45}_{-0.23}$
Backg.	$0.199^{+0.074}_{-0.082}$ $0.184^{+0.099}_{-0.081}$	$11.2^{+4.5}_{-3.2}$	[b] $28.88^{+0.90}_{-2.1}$	$51.33^{+5.20}_{-3.75}$	$13.2^{+6.3}_{-4.1}$	394^{+91}_{-88}	30^{+21}_{-13}	$42.7^{+6.3}_{-5.5}$	$3.86^{+0.62}_{-0.58}$

Notes. The main value refers to the 50% percentile, while the errors refer to the deviation to the 16th and 84th percentiles. [a] The values in the first and second rows refer to the energy fraction absorbed by the ISM as estimated from stellar-dominated (f_μ^{SFH}) and dust-dominated (f_μ^{IR}) photometry. [b] The T^{ISM} PDF for the background source does not reach a peak, so value should not be considered reliable.

to ALMA band 8, which was not available during Cycle 0, preventing an estimate of T_{ex}. Hence, we again assume the value estimated by MBB_EMCEE in the optically-thin case ($35.9^{+4.3}_{-4.3}$ K, Table 6). For $L'_{\mathrm{C\,I(^3P_1 \to {}^3P_0)}} = 4.15 \pm 0.60 \times 10^{10}\,\mu^{-1}$ K km s^{-1} pc^2, we estimate a lower limit of $M_{\mathrm{CI}} > 5.23^{+0.76}_{-0.76} \times 10^7\,\mu^{-1}\,M_\odot$. Weiß et al. (2005) found, for a sample of three $z \sim 2.5$ sources, a

carbon abundance of $X[\mathrm{C\,I}]/X[\mathrm{H}_2] = M_{\mathrm{CI}}/(6\,M_{\mathrm{H}_2}) \sim 5 \times 10^{-5}$, which is roughly double that found in our Galaxy (2.2×10^{-5}, Frerking et al. 1989). We note that the reported M_{H_2} masses in Weiß et al. (2005) were estimated based on CO emission assuming $X_{\mathrm{CO}}^{\mathrm{thin}} = 0.8$, and the carbon abundance in our Galaxy is likely not representative of that in H1429−0028. We assume the Galactic value provides an upper limit instead. Hence, assuming

Table 6. FIR-to-mm properties of H1429−0028.

Case	Thin	Thick
T [K]	$35.9^{+4.3}_{-4.3}$	73^{+13}_{-23}
α^a	$7.6^{+7.5}_{-6.5}$	$8.3^{+6.6}_{-5.6}$
β^b	$2.14^{+0.23}_{-0.24}$	$2.25^{+0.61}_{-0.65}$
λ_0 [μm]^c	–	779^{+986}_{-405}
$M_{\rm dust}$ $\left[10^8\,M_\odot\right]$	$5.2^{+1.9}_{-2.6}$	$4.9^{+1.8}_{-3.5}$
$L_{8-1000\,\mu m}$ $\left[10^{12}\,L_\odot\right]$	$6.2^{+2.5}_{-2.2}$	$4.9^{+1.7}_{-3.1}$
ν^d	2	1
χ^2	1.94	0.62

Notes. Photometry analysis with MBB_EMCEE using only *Herschel* 100−500-μm and ALMA 1.28-mm data. Errors are $\pm 1\sigma$. The MBB_EMCEE analysis considers a covariance matrix to account for flux calibration issues and uncertainty. $^{(a)}$ The mid-IR power-law index. $^{(b)}$ The extinction curve power-law index. β was limited to values below 3. $^{(c)}$ Wavelength at which optical depth equals unity. λ_0 was limited to values below 2000 μm. $^{(d)}$ Number of degrees of freedom. This is the number of photometric data points used (six), minus the number of parameters to fit in each case, four and five, respectively, for the optically thin and thick cases (T, α, β, normalisation, λ_0).

the range of X[C I]$/X$[H$_2$] values, we expect the intrinsic molecular mass to be in the range $1.80_{-0.29} < M_{\rm H_2}/10^{10}\,[M_\odot] < 4.08^{+0.66}$.

Finally, Scoville et al. (2014) propose an empirical approach to estimate total ISM gas mass ($M_{\rm H\,I} + M_{\rm H_2}$) based on submm continuum emission. The relation is calibrated with a sample of local galaxies for which global $M_{\rm H\,I}$ and $M_{\rm H_2}$ estimates as well as submm observations exist. The reference wavelength is set at rest-frame $850\,\mu$m, which traces the Rayleigh-Jeans tail of an SED. The relation is the following:

$$M_{\rm ISM} = 1.2 \times 10^4\, D_{\rm L}^2 \left(\frac{350}{\nu_{\rm obs}}\right)^\beta (1+z)^{-(1+\beta)}\, S_{\nu_{\rm obs}}\, \mu^{-1},$$

where $[M_{\rm ISM}] = M_\odot$, $[D_{\rm L}] = {\rm Mpc}$, $[S_{\nu_{\rm obs}}] = {\rm mJy}$, $[\nu_{\rm obs}] = {\rm GHz}$ (350 corresponds to the frequency in GHz at $850\,\mu$m), β is the FIR−mm power-law index ($\beta = 3.89 \pm 0.41$ in our case, Section 3.6). Hence, adopting our 1.28-mm flux density estimate of 5.86 ± 0.99 mJy and a magnification of $\mu = 10.8 \pm 0.7$, the estimated intrinsic ISM gas mass is $M_{\rm ISM} = 4.6 \pm 1.7 \times 10^{10}\,M_\odot$ (with a conservative 25% uncertainty added in quadrature due to the expected scatter of the adopted relation, Scoville et al. 2014). This means a molecular-to-total gas mass ratio of $0.39_{-0.16} < M_{\rm H2}/M_{\rm ISM} < 0.89^{+0.11}$, a gas-to-baryonic mass fraction of $0.26^{+0.15}_{-0.13}$, and a depletion time of $\tau_{\rm SF} = M_{\rm ISM}/SFR = 117^{+51}_{-51}$ Myr. This timescale is in agreement with that expected for the SMG phase (~ 100 Myr, Greve et al. 2004; Tacconi et al. 2006, 2008; Ivison et al. 2011). However, despite the evidence of a high-density and dusty environment (the detection of CS $10 \rightarrow 9$ and $M_{\rm dust} = 3.86^{+0.62}_{-0.58} \times 10^8\,M_\odot$), which could make H_2 formation easier (Krumholz 2014, and references therein), such a short timescale and the fact that star formation is more directly related to molecular gas and not so much to total gas, or more specifically, neutral gas (Elmegreen 2011, and references therein), may imply a much shorter starburst phase, in the range $46_{-13} < M_{\rm H_2}/SFR < 104^{+29}$ Myr, and a longer depletion time.

4.5. Comparing dynamical and SED masses

In Sections 4.1.3, 4.2 and 4.4, we show that the expected background dynamical and baryonic masses are, respectively, $5.8 \pm 1.7 \times 10^{10}\,M_\odot$ and $17.8^{+6.5}_{-4.4} \times 10^{10}\,M_\odot$. If, for the latter, one considers a $20 \pm 10\%$ contribution from dark matter (Gerhard et al. 2001; Kassin et al. 2006; Daddi et al. 2010a), $22.3^{+8.3}_{-5.8} \times 10^{10}\,M_\odot$, there is a significant tension between the mass estimates obtained via the dynamical and SED data. The point driving this discrepancy is the fact that the dynamical information traced by the CO (J:4 → 3) emission is dominated by the north-south component, whereas the SED information comes from the system as a whole, thus including the east-west component. As a result, one may estimate the dynamical mass of the east-west component by assuming it is the difference between the SED-derived total mass and the north-south component dynamical mass. Such an assumption implies a dynamical mass of $16.5^{+8.5}_{-6.0} \times 10^{10}\,M_\odot$ for the east-west component. This means we may be witnessing a 1:$2.8^{+1.8}_{-1.5}$ intermediate-to-major merger at $z = 1.027$.

5. Conclusions

This work focus on a *Herschel* 500-μm-selected source, HATLAS J142935.3−002836 (H1429−0028), a candidate lensed galaxy. The lensing scenario is confirmed with the help of multi-wavelength, high-resolution imaging (Fig. 1) which reveals a foreground edge-on disk galaxy surrounded by an almost complete Einstein ring.

Optical and FIR spectroscopy allow to measure, respectively, a foreground redshift of $z_{\rm sp} = 0.218$ and a background redshift of $z_{\rm sp} = 1.027$.

A semi-linear inversion (SLI) algorithm (Warren & Dye 2003; Dye et al. 2014), which does not assume any a priori background morphology and allows multiple images to be simultaneously reconstructed using the same lens mass model, is adopted to characterise the lens. This is done making use of 7-GHz continuum and velocity-integrated CO (J:4 → 3) flux maps. The total and stellar masses within the Einstein radius ($\theta_{\rm E} = 2.18^{+0.19}_{-0.27}$ kpc) are estimated to be, respectively, $M(<\theta_{\rm E}) = 8.13^{+0.33}_{-0.41} \times 10^{10}\,M_\odot$ and $1.60^{+1.14}_{-0.69} \times 10^{10}\,M_\odot$, yielding a stellar mass contribution to the deflection effect of $19.7^{+14.1}_{-8.5}\%$.

The same algorithm is utilised to reconstruct the source plane at different wavelengths. The background source is magnified by $\mu \sim 8-10$ (depending on wavelength) and is likely a merger event between two sources oriented respectively north-south (NS) and east-west (EW), with a projection angle between the two of ~ 80 deg. There is also evidence of a tidal tail spanning tens of kpc, resembling the Antennæ merger (Figs. 8 and 9).

The dynamical analysis, based on our source-plane CO (J:4 → 3) cube, allows us to observe that one of the components, despite showing some evidence of rotation (with the south emission being mostly blueshifted, and the north emission being partly redshifted), is morphologically disturbed (Sec. 4.1.3). The tension between dark plus baryonic mass ($22.3^{+8.3}_{-5.8} \times 10^{10}\,M_\odot$) and the dynamical mass ($5.8 \pm 1.7 \times 10^{10}\,M_\odot$) estimated for the background source results from the dynamical analysis being sensitive to the NS component alone, as the EW component remains undetected in CO (J:4 → 3) and 1.28-mm continuum maps. This tension was then used to estimate the dynamical mass of the EW component ($16.5^{+8.5}_{-6.0} \times 10^{10}\,M_\odot$) and infer a merger mass-ratio of 1:$2.8^{+1.8}_{-1.5}$ (Sect. 4.5).

The system as a whole has a stellar mass of $1.32^{+0.63}_{-0.41} \times 10^{11}\,M_\odot$, it is actively forming stars (SFR of $394^{+91}_{-88}\,M_\odot$ yr^{-1}

and specific SFR of $3.0^{+2.1}_{-1.3}$ Gyr^{-1}, Sect. 4.2), and has a significant gas reservoir in its ISM ($4.6 \pm 1.7 \times 10^{10}\,M_\odot$ comprising $\sim$25% of the baryonic mass, Sec. 4.4). This implies a depletion time due to star formation alone of $\tau_{SF} = 117^{+51}_{-51}$ Myr, which is in agreement with that expected for the SMG phase ($\sim$100 Myr, e.g., Tacconi et al. 2006).

The comparison between SFRs computed via FIR/millimetre and radio estimators yields no strong evidence of active galactic nucleus activity.

Thanks to a plethora of multi-wavelength datasets, it was possible to have a first glimpse of the properties of H1429−0028. A glimpse of time was what actually took ALMA − still in Cycle-0 − to provide the rich set of information at mm wavelengths, showing how efficient can be the teaming of *Herschel*-ATLAS with ALMA to find and study these rare, fortuitous events, enabling the unprecedented detailed assessment of galaxy mass assembly mechanisms with cosmic time.

References

Ahn, C. P., Alexandroff, R., Allende Prieto, C., et al. 2012, ApJS, 203, 21
Bell, E. F. 2003, ApJ, 586, 794
Blain, A. W. 1996, MNRAS, 283, 1340
Blain, A. W., Smail, I., Ivison, R. J., & Kneib, J.-P., MNRAS, 302, 632
Bock, D. C.-J., Bolatto, A. D., Hawkins, D. W., et al. 2006, Proc. SPIE, 6267
Bradford, C. M., Aguirre, J. E., Bock, J. J., et al. 2009, Submillimeter Astrophysics and Technology: a Symposium Honoring Thomas G. Phillips, 417, 341
Braine, J., Combes, F., Casoli, F., et al. 1993, A&AS, 97, 887
Bruzual, G., & Charlot, S. 2003, MNRAS, 344, 1000
Bryant, P. M., & Scoville, N. Z. 1996, ApJ, 457, 678
Burigana, C., & Popa, L. 1998, A&A, 334, 420
Bussmann, R. S., Gurwell, M. A., Fu, H., et al. 2012, ApJ, 756, 134
Bussmann, R. S., Pérez-Fournon, I., Amber, S., et al. 2013, ApJ, 779, 25
Calanog, J. A., Fu, H., Cooray, A., et al. 2014, ApJ, submitted [arXiv:1406.1487]
Carilli, C., & Walter, F. 2013, ARA&A, 51, 105
Carilli, C. L., Daddi, E., Riechers, D., et al. 2010, ApJ, 714, 1407
Casey, C. M., Narayanan, D., & Cooray, A. 2014, Phys. Rep., accepted [arXiv:1402.1456]
Chapman, S. C., Smail, I., Ivison, R. J., & Blain, A. W. 2002, MNRAS, 335, L17
Chapman, S. C., Blain, A. W., Smail, I., & Ivison, R. J. 2005, ApJ, 622, 772
Clements, D. L., Rigby, E., Maddox, S., et al. 2010, A&A, 518, L8
Clemens, M. S., Negrello, M., De Zotti, G., et al. 2013, MNRAS, 433, 695
Condon, J. J. 1992, ARA&A, 30, 575
Conley, A., Cooray, A., Vieira, J. D., et al. 2011, ApJ, 732, L35
Coppin, K., Halpern, M., Scott, D., et al. 2008, MNRAS, 384, 1597
Cox, P., Krips, M., Neri, R., et al. 2011, ApJ, 740, 63
da Cunha, E., Charlot, S., & Elbaz, D. 2008, MNRAS, 388, 1595
Daddi, E., Bournaud, F., Walter, F., et al. 2010a, ApJ, 713, 686
Daddi, E., Elbaz, D., Walter, F., et al. 2010b, ApJ, 714, L118
Dannerbauer, H., Daddi, E., Morrison, G. E., et al. 2010, ApJ, 720, L144
Davé, R., Finlator, K., Oppenheimer, B. D., et al. 2010, MNRAS, 404, 1355
Díaz-Santos, T., Armus, L., Charmandaris, V., et al. 2013, ApJ, 774, 68
Draine, B. T., Dale, D. A., Bendo, G., et al. 2007, ApJ, 663, 866
Dye, S., Negrello, M., Hopwood, R., et al. 2014, MNRAS, 440, 2013
Eales, S., Dunne, L., Clements, D., et al. 2010, PASP, 122, 499
Elmegreen, B. G. 2011, EAS Pub. Ser., 51, 3
Engel, H., Tacconi, L. J., Davies, R. I., et al. 2010, ApJ, 724, 233
Fall, S. M., Charlot, S., & Pei, Y. C. 1996, ApJ, 464, L43
Fazio, G. G., Hora, J. L., Allen, L. E., et al. 2004, ApJS, 154, 10
Fixsen, D. J., Dwek, E., Mather, J. C., Bennett, C. L., & Shafer, R. A. 1998, ApJ, 508, 123
Fixsen, D. J., Bennett, C. L., & Mather, J. C. 1999, ApJ, 526, 207
Foreman-Mackey, D., Hogg, D. W., Lang, D., & Goodman, J. 2013, PASP, 125, 306
Förster Schreiber, N. M., Genzel, R., Bouché, N., et al. 2009, ApJ, 706, 1364
Förster Schreiber, N. M., Shapley, A. E., Erb, D. K., et al. 2011, ApJ, 731, 65
Franceschini, A., Mazzei, P., de Zotti, G., & Danese, L. 1994, ApJ, 427, 140

Frayer, D. T., Ivison, R. J., Scoville, N. Z., et al. 1998, ApJ, 506, L7
Frayer, D. T., Ivison, R. J., Scoville, N. Z., et al. 1999, ApJ, 514, L13
Frayer, D. T., Harris, A. I., Baker, A. J., et al. 2011, ApJ, 726, L22
Frerking, M. A., Keene, J., Blake, G. A., & Phillips, T. G. 1989, ApJ, 344, 311
Fu, H., Jullo, E., Cooray, A., et al. 2012, ApJ, 753, 134
Fu, H., Cooray, A., Feruglio, C., et al. 2013, Nature, 498, 338
Furlanetto, C., Santiago, B. X., Makler, M., et al. 2013, MNRAS, 1144
George, R. D., Ivison, R. J., Hopwood, R., et al. 2013, MNRAS, 436, L99
George, R., Ivison, R., Smail, I., et al. 2014, MNRAS, 442, 1877
Gerhard, O., Kronawitter, A., Saglia, R. P., & Bender, R. 2001, AJ, 121, 1936
González, J. E., Lacey, C. G., Baugh, C. M., & Frenk, C. S. 2011, MNRAS, 413, 749
Granato, G. L., De Zotti, G., Silva, L., Bressan, A., & Danese, L. 2004, ApJ, 600, 580
Greve, T. R., Ivison, R. J., Bertoldi, F., et al. 2004, MNRAS, 354, 779
Greve, T. R., Bertoldi, F., Smail, I., et al. 2005, MNRAS, 359, 1165
Greve, T. R., Pope, A., Scott, D., et al. 2008, MNRAS, 389, 1489
Harris, A. I., Baker, A. J., Frayer, D. T., et al. 2012, ApJ, 752, 152
Hauser, M. G., & Dwek, E. 2001, ARA&A, 39, 249
Hayward, C. C., Kereš, D., Jonsson, P., et al. 2011, ApJ, 743, 159
Hodge, J. A., Carilli, C. L., Walter, F., et al. 2012, ApJ, 760, 11
Hodge, J. A., Karim, A., Smail, I., et al. 2013, ApJ, 768, 91
Hughes, D. H., Serjeant, S., Dunlop, J., et al. 1998, Nature, 394, 241
Ibar, E., Ivison, R. J., Cava, A., et al. 2010a, MNRAS, 409, 38
Ibar, E., Ivison, R. J., Best, P. N., et al. 2010b, MNRAS, 401, L53
Ivison, R. J., Smail, I., Barger, A. J., et al. 2000, MNRAS, 315, 209
Ivison, R. J., Swinbank, A. M., Swinyard, B., et al. 2010, A&A, 518, L35
Ivison, R. J., Papadopoulos, P. P., Smail, I., et al. 2011, MNRAS, 412, 1913
Ivison, R. J., Swinbank, A. M., Smail, I., et al. 2013, ApJ, 772, 137
Jacobs, B. A., Sanders, D. B., Rupke, D. S. N., et al. 2011, AJ, 141, 110
Karim, A., Swinbank, M., Hodge, J., et al. 2012, MNRAS, 432, 2
Kassin, S. A., de Jong, R. S., & Weiner, B. J. 2006, ApJ, 643, 804
Kassiola, A., & Kovner, I. 1993, ApJ, 417, 474
Keeton, C. R. 2001 [arXiv:astro-ph/0102340]
Kennicutt, R. C., Jr. 1998, ARA&A, 36, 189
Kereš, D., Katz, N., Weinberg, D. H., & Davé, R. 2005, MNRAS, 363, 2
Kneib, J.-P., Neri, R., Smail, I., et al. 2005, A&A, 434, 819
Knudsen, K. K., Barnard, V. E., van der Werf, P. P., et al. 2006, MNRAS, 368, 487
Kormann, R., Schneider, P., & Bartelmann, M. 1994, A&A, 284, 285
Krumholz, M. R. 2014 [arXiv:1402.0867]
Lagache, G., Abergel, A., Boulanger, F., Désert, F. X., & Puget, J.-L. 1999, A&A, 344, 322
Lapi, A., González-Nuevo, J., Fan, L., et al. 2011, ApJ, 742, 24
Lupu, R. E., Scott, K. S., Aguirre, J. E., et al. 2012, ApJ, 757, 135
Magnelli, B., Elbaz, D., Chary, R. R., et al. 2009, A&A, 496, 57
Makovoz, D., & Marleau, F. R. 2005, PASP, 117, 1113
Mao, R.-Q., Schulz, A., Henkel, C., et al. 2010, ApJ, 724, 1336
Marigo, P., & Girardi, L. 2007, A&A, 469, 239
Menéndez-Delmestre, K., Blain, A. W., Swinbank, M., et al. 2013, ApJ, 767, 151
Meylan, G., Jetzer, P., North, P., et al. 2006, Saas-Fee Advanced Course 33: Gravitational Lensing: Strong, Weak and Micro
Michałowski, M. J., Watson, D., & Hjorth, J. 2010a, ApJ, 712, 942
Michałowski, M., Hjorth, J., & Watson, D. 2010b, A&A, 514, A67
Mortier, A. M. J., Serjeant, S., Dunlop, J. S., et al. 2005, MNRAS, 363, 563
Narayanan, D., Krumholz, M. R., Ostriker, E. C., & Hernquist, L. 2012, MNRAS, 421, 3127
Negrello, M., Hopwood, R., De Zotti, G., et al. 2010, Science, 330, 800
Pascale, E., Auld, R., Dariush, A., et al. 2011, MNRAS, 415, 911
Peng, C. Y., Ho, L. C., Impey, C. D., & Rix, H.-W. 2010, AJ, 139, 2097
Postman, M., Coe, D., Benítez, N., et al. 2012, ApJS, 199, 25
Puget, J.-L., Abergel, A., Bernard, J.-P., et al. 1996, A&A, 308, L5
Reach, W. T., Dwek, E., Fixsen, D. J., et al. 1995, ApJ, 451, 188
Renzini, A. 2006, ARA&A, 44, 141
Riechers, D. A., Hodge, J., Walter, F., Carilli, C. L., & Bertoldi, F. 2011, ApJ, 739, L31
Riechers, D. A., Bradford, C. M., Clements, D. L., et al. 2013, Nature, 496, 329
Rigby, E. E., Maddox, S. J., Dunne, L., et al. 2011, MNRAS, 415, 2336
Rowlands, K., Gomez, H. L., Dunne, L., et al. 2014, MNRAS, 441, 1040
Saunders, W. 1990, Ph.D. Thesis, Queen Mary College, University of London, 353
Saunders, W., Rowan-Robinson, M., Lawrence, A., et al. 1990, MNRAS, 242, 318
Schneider, P., Ehlers, J., & Falco, E. E. 1992, Gravitational Lenses, XIV (Berlin, Heidelberg, New York: Springer-Verlag), Astron. Astrophys. Lib., 560, 112

Scott, S. E., Fox, M. J., Dunlop, J. S., et al. 2002, MNRAS, 331, 817
Scott, K. S., Lupu, R. E., Aguirre, J. E., et al. 2011, ApJ, 733, 29
Scoville, N., Aussel, H., Sheth, K., et al. 2014, ApJ, 783, 84
Sersic, J. L. 1968, Atlas de galaxias australes (Cordoba, Argentina: Observatorio Astronomico)
Smail, I., Ivison, R. J., & Blain, A. W. 1997, ApJ, 490, L5
Smail, I., Ivison, R. J., Blain, A. W., & Kneib, J.-P. 2002, MNRAS, 331, 495
Smail, I., Swinbank, A. M., Ivison, R. J., & Ibar, E. 2011, MNRAS, 414, L95
Smolčić, V., Navarrete, F., Aravena, M., et al. 2012, ApJS, 200, 10
Solomon, P. M., & Barrett, J. W. 1991, in Dynamics of Galaxies and Their Molecular Cloud Distributions, Proc. IAU Symp. 146, 235
Solomon, P. M., & Vanden Bout, P. A. 2005, ARA&A, 43, 677
Solomon, P. M., Rivolo, A. R., Barrett, J., & Yahil, A. 1987, ApJ, 319, 730
Solomon, P. M., Downes, D., Radford, S. J. E., & Barrett, J. W. 1997, ApJ, 478, 144
Sutherland, W. 2012, in Science from the Next Generation Imaging and Spectroscopic Surveys, 40
Suyu, S. H., Marshall, P. J., Hobson, M. P., & Blandford, R. D. 2006, MNRAS, 371, 983
Swinbank, A. M., Smail, I., Longmore, S., et al. 2010, Nature, 464, 733
Swinbank, A. M., Papadopoulos, P. P., Cox, P., et al. 2011, ApJ, 742, 11
Tacconi, L. J., Neri, R., Chapman, S. C., et al. 2006, ApJ, 640, 228
Tacconi, L. J., Genzel, R., Smail, I., et al. 2008, ApJ, 680, 246
Tacconi, L. J., Genzel, R., Neri, R., et al. 2010, Nature, 463, 781
Thomson, A. P., Ivison, R. J., Smail, I., et al. 2012, MNRAS, 425, 2203
Thomson, A. P., Ivison, R. J., Simpson, J. M., et al. 2014, MNRAS, submitted [arXiv:1404.7128]
Vieira, J. D., Marrone, D. P., Chapman, S. C., et al. 2013, Nature, 495, 344
Wardlow, J. L., Smail, I., Coppin, K. E. K., et al. 2011, MNRAS, 415, 1479
Wardlow, J. L., Cooray, A., De Bernardis, F., et al. 2013, ApJ, 762, 59
Warren, S. J., & Dye, S. 2003, ApJ, 590, 673
Weiß, A., Downes, D., Henkel, C., & Walter, F. 2005, A&A, 429, L25
Weiß, A., De Breuck, C., Marrone, D. P., et al. 2013, ApJ, 767, 88
Werner, M. W., Roellig, T. L., Low, F. J., et al. 2004, ApJS, 154, 1
Wizinowich, P. L., Le Mignant, D., Bouchez, A. H., et al. 2006, PASP, 118, 297
Wright, E. L., Eisenhardt, P. R. M., Mainzer, A. K., et al. 2010, AJ, 140, 1868
York, D. G., Adelman, J., Anderson, J. E., Jr., et al. 2000, AJ, 120, 1579
Yun, M. S., Reddy, N. A., & Condon, J. J. 2001, ApJ, 554, 803
Yun, M. S., Scott, K. S., Guo, Y., et al. 2012, MNRAS, 420, 957
Zemcov, M., Aguirre, J., Bock, J., et al. 2012, ApJ, 749, 114
Zylka, R. 1998, The MOPSI Cookbook (Bonn: MPIfR), http://www.mpifr-bonn.mpg.de/staff/bertoldi/mambo/

[1] Universidad de Concepción, Barrio Universitario, Concepción, Chile
[2] Centro de Astronomia e Astrofísica da Universidade de Lisboa, Observatório Astronómico de Lisboa, Tapada da Ajuda, 1349-018 Lisbon, Portugal
e-mail: hmessias@oal.ul.pt
[3] School of Physics and Astronomy, University of Nottingham, NG7 2RD, UK
[4] Harvard-Smithsonian Center for Astrophysics, 60 Garden Street, Cambridge, MA 02138, USA
[5] Department of Physics & Astronomy, University of California, Irvine, CA 92697, USA
[6] Universitä Wien, Institut für Astrophysik, Türkenschanzstraß e 17, 1180 Wien, Austria
[7] Department of Physics and Astronomy, University of Iowa, Iowa City, IA 52242, USA
[8] Instituto de Física y Astronomía, Universidad de Valparaíso, Avda. Gran Bretaña 1111, Valparaíso, Chile
[9] Institute for Astronomy, University of Edinburgh, Royal Observatory, Blackford Hill, Edinburgh EH9 3HJ, UK
[10] European Southern Observatory, Karl Schwarzschild Strasse 2, Garching, Germany
[11] INAF, Osservatorio Astronomico di Padova, Vicolo Osservatorio 5, 35122 Padova, Italy
[12] Astronomy Department, California Institute of Technology, MC 249-17, 1200 East California Boulevard, Pasadena, CA 91125, USA
[13] Department of Astronomy, Cornell University, Ithaca, NY 14853, USA

[14] Department of Physics and Astronomy, University of Pennsylvania, Philadelphia, PA 19104, USA

[15] The Open University, PO Box 197, Milton Keynes, MK7 6BJ, UK

[16] HH Wills Physics Laboratory, University of Bristol, Tyndall Avenue, Bristol BS8 1TL, UK

[17] Harvard-Smithsonian Center for Astrophysics, 60 Garden Street, Cambridge, MA 02138, USA

[18] Jet Propulsion Laboratory, California Institute of Technology, 4800 Oak Grove Drive, Pasadena, CA 91109, USA

[19] Astrophysics Group, Imperial College London, Blackett Laboratory, Prince Consort Road, London SW7 2AZ, UK

[20] Department of Physics and Astronomy, University of Canterbury, Private Bag 4800, 8140 Christchurch, New Zealand

[21] School of Physics and Astronomy, Cardiff University, QueensBuildings, The Parade, Cardiff CF24 3AA, UK

[22] School of Mathematical Sciences, Queen Mary, University of London, Mile End Road, London, E1 4NS, UK

[23] University of Colorado at Boulder, Center for Astrophysics and Space Astronomy, 389-UCB, Boulder, CO, USA

[24] Steward Observatory, University of Arizona, 933 North Cherry Avenue, Tucson, AZ 85721, USA

[25] Infrared Processing and Analysis Center, California Institute of Technology, MC 314-6, Pasadena, CA 91125, USA

[26] Institut d'Astrophysique de Paris, UMR 7095, CNRS, UPMC Univ. Paris 06, 98bis boulevard Arago, 75014 Paris, France

[27] (SUPA) School of Physics & Astronomy, University of St Andrews, North Haugh, St Andrews, KY16 9SS, UK

[28] Centre for Astrophysics Research, Science & Technology Research Institute, University of Hertfordshire, Herts AL10 9AB, UK

[29] Department of Astronomy and Department of Physics, University of Illinois, 1002 West Green Street, Urbana, IL 61801, USA